Chapter 1

Examples of a Pool Boiling Simulations Using an Interface Tracking Method Applied to Nucleate Boiling, Departure from Nucleate Boiling and Film Boiling

Yohei Sato, Brian L. Smith, Bojan Niceno

Paul Scherrer Institute, Nuclear Energy and Safety Department,
Villigen PSI, 5232, Switzerland
yohei.sato@psi.ch

Several pool-boiling calculations are presented as examples of a numerical modeling approach to two-phase heat transfer using Computational Fluid Dynamics (CFD). A specific feature of the method described is its applicability to a wide range of boiling regimes: nucleate boiling, departure from nucleation boiling, and film boiling. It is shown that the overall boiling heat-transfer coefficient may be predicted accurately by incorporating: (i) tracking of the liquid/vapor interface, (ii) a random nucleation site model, and (iii) a micro-layer model of the liquid film assumed to be present between each emerging bubble and the underlying heat-transfer surface. The numerical simulation is capable of providing quantitative data characterizing the physical phenomena involved: namely, estimates of the separate contributions to the total mass and heat transfer rates, which individually would be difficult to distinguish using experiments alone. Simulations of this type require very fine grid resolution to capture the liquid-vapor interface accurately, and our simulations are no exception: indeed, hundreds of CPUs are needed to obtain a solution. Nonetheless, interface tracking promises attractive future prospects in pool-boiling modeling, since it has the capability to calculate phase-change without the involvement of empirical models.

1. Introduction

In this chapter, we present an example of how CFD can be used to simulate boiling flow in combination with an interface tracking method. An overview of the CFD simulation approach to boiling flow can be found in the Encyclopedia of Two-Phase Heat Transfer and Flow II; Volume 4, the final objective being to derive a complete, mechanistic understanding of all boiling phenomena,

including those leading to Critical Heat Flux (CHF) on heat-transfer surfaces. To this purpose, numerical modelling approaches, which aim to reproduce the phenomena without the involvement of empirical models, need to be developed. Key numerical modelling in boiling simulation are considered to be:

- highly resolved liquid-vapor interface modelling,
- phase-change modelling based on energy balance equation,
- treatment of micro-layer, and
- conjugate heat transfer between fluid and solid phases.

Since phase-change occurs at the liquid-vapor interface, the interface shape must be captured with sufficient resolution. There are several methods available: interface-tracking methods, the phase-field method, the lattice Boltzmann method; these different approaches are reviewed in this Encyclopedia by Mukherjee and Dhir [2015]. Our approach is to use an interface tracking method based on the color function [Sato and Niceno, 2012a]. The color function represents the volume fraction of liquid in any given control volume, in much the same way as the Volume Of Fluid (VOF) method [Hirt and Nichols, 1981], and ensuring that mass-conservation is always satisfied. Compared to VOF, our method is simple in terms of surface re-construction: in our scheme, only one equation, called the *sharpening equation*, is required to be solved to prevent smearing of the color function, while typically, in the Piecewise Linear Interface Calculation (PLIC) [Youngs, 1982], which entails complicated programming procedures, must be used in VOF. In our model, Brackbill's Continuum Surface Force (CSF) model [Brackbill *et al.*, 1992] is employed to represent the surface-tension effect, and it is coupled with the color function method as described by Sato and Niceno [2012b].

The modelling of phase-change is also essential, since the mass-transfer rate has to be explicitly calculated in our model. The sharp-interface/phase-change model [Sato and Niceno, 2013] is used to this purpose. In this model, the phase-change occurs only in a control volume which includes the physical liquid-vapor interface, and the model is accurate even for cases with a high density ratio between liquid and vapor; the model takes into account both superheated liquid and supercooled vapor.

The main difficulty of using CFD to simulate nucleate boiling lies in the treatment of the micro-layer, which is a thin liquid film existing beneath a growing bubble. The existence of micro-layer was confirmed experimentally using optical interferometry by Sharp [1964], and by Jawurek [1969] in the 1960's. These pioneering works were followed by several others [Voutsinos and Judd, 1975; Koffman and Plesset, 1983; Utaka *et al.*, 2013], all reaching similar conclusions. These works revealed that the initial thickness of the micro-layer is of the order of few micrometers, and the thickness decreases as the liquid layer

vaporizes. Massive vaporization takes place at the upper surface of the micro-layer, driven by the high heat flux through the layer. The high temperature gradient associated with this heat flux is the result of: (i) the thinness of the layer, and (ii) the large temperature difference between the top and the bottom of the layer, the latter in touch with the heat-transfer surface. In order to numerically simulate a micro-layer, whose thickness finally approaches zero, sub-grid-scale modelling is required. The authors have developed such a sub-grid model, named *depletable micro-layer model*; details are given in Sato and Niceno [2015]. Using this model, the micro-layer is able to vaporize completely, thus resulting in the creation of a dry spot underneath the bubble, as illustrated schematically in Fig. 1.
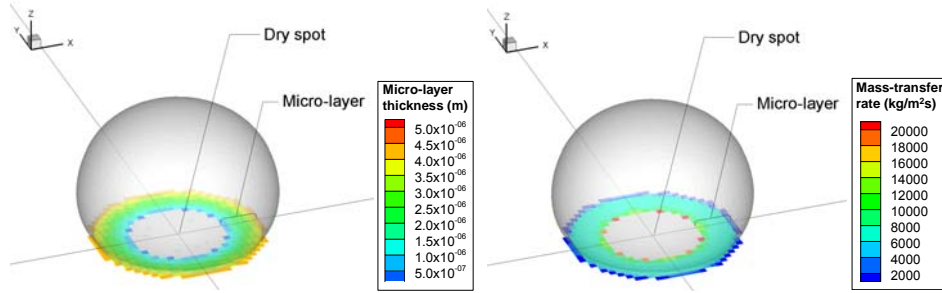

Fig. 1. Typical distributions of the micro-layer thickness (left) and the mass-transfer rate (right) on a heat-transfer surface during bubble growth as computed using the *depletable micro-layer model* of Sato and Niceno [2015].

The modeling of conjugate heat transfer between the solid and fluid domains is necessary to accurately predict the temperature field in the solid domain and the heat flux over the heat-transfer surface. We strictly take into account conjugate heat transfer, and, based on the computed temperature at any nucleation site, the nucleation site is activated by planting a tiny hemispherical bubble at the site.

The boiling regimes considered are nucleate boiling, Departure from Nucleate Boiling (DNB), and film boiling. These boiling regimes are simulated using the same numerical method without changing parameters. All the results of the simulations undertaken are compared with corresponding experimental data. In this Chapter, we focus only on pool boiling at atmospheric pressure, but our pool boiling simulations at high pressure, and convective boiling simulations, are reported in Refs. [Murallidharan *et al.*, 2016; Sato *et al.*, 2013; Lal *et al.*, 2015]. The supercomputer at the Swiss National Supercomputing Center was used to accelerate the throughput for all the simulations.

The structure of the rest of this Chapter is as follows: in Sec. 2, the numerical approach adopted is explained in detail. The verification and validation test cases undertaken in support of our modeling approach are described in Sec. 3, Closure of the Chapter is given in Sec. 4.

2. Numerical method

2.1. *Navier-Stokes solver for two-phase flow*

The incompressible Navier-Stokes equations are solved using a finite-volume approach on a fixed, rectangular, Cartesian grid using the projection method [Chorin, 1968]. A staggered-variable arrangement [Harlow and Welch, 1965] is adopted, with the vector velocity and body-force components defined on cell faces, and the scalar variables − pressure, temperature, color function and phase-change rate − defined at cell centers. The spatial discretization is based on a second-order-accurate, upwind scheme for the advection terms, and a second-order, central-difference scheme for the diffusion terms. Although a central difference scheme would be more desirable for the advection terms, since it would then be unbiased, we use an upwind scheme here to avoid the numerical instabilities associated with the central-differencing scheme. The time discretization is first-order implicit for the diffusion terms, and first-order explicit for the advection terms. A first-order scheme is employed for the time discretization, instead of a second-order scheme (such as Adams-Bashforth (AB)), again to ensure numerical stability of the solution algorithm. In phase-change simulations involving a moving liquid-vapor interface, and high liquid-vapor density ratio, the velocity change in time around the liquid-vapor interface becomes large and discontinuous as the interface crosses the points at which the velocity components are defined (i.e. at the centers of the cell faces in our case). Since second-order schemes such as AB use values at both the previous and current time steps to predict the value at the next time step, based on a Taylor-series expansion, assuming continuous variation of quantities. Such schemes are deemed unsuitable for simulations in which there are discontinuous velocity changes.

The governing equations for mass and momentum conservation may be written as follows:

$$\frac{\partial \rho}{\partial t} + \nabla \cdot \left(\rho \vec{u} \right) = 0 , \tag{1}$$

$$\frac{\partial(\rho\vec{u})}{\partial t}+\nabla\cdot(\rho\vec{u}\vec{u})=-\nabla p+\nabla\cdot\left\{(\mu+\mu_t)\left(\nabla\vec{u}+(\nabla\vec{u})^T\right)\right\}+\vec{f}\,, \tag{2}$$

where $\vec{u}$ (m/s) is the velocity vector, ρ (kg/m^3) the density, t (s) the time, p (Pa) the pressure, μ ($Pa{\cdot}s$) the dynamic molecular viscosity, μ_t ($Pa{\cdot}s$) the turbulent eddy viscosity, and $\vec{f}$ (N/m^3) the body-force vector. Turbulence is modeled using Large Eddy Simulation (LES), the Smagorinsky subgrid-scale model [Smagorinsky, 1963] being adopted to estimate the turbulent eddy viscosity; a Smagorinsky constant of $C_s = 0.17$ is employed here. Note that the interaction between the turbulence and the liquid-vapor interface is not taken into account in the present implementation. Note that in the case of Direct Numerical Simulation (DNS), μ_t is set to zero.

In our solution procedure, Eqs. (1)-(2) are first rewritten as follows:

$$\nabla\cdot\vec{u}=\left(\frac{1}{\rho_v}-\frac{1}{\rho_l}\right)\dot{m}\,, \tag{3}$$

$$\rho\frac{\partial\vec{u}}{\partial t}+\rho\left\{\nabla\cdot(\vec{u}\vec{u})-\vec{u}(\nabla\cdot\vec{u})\right\}=-\nabla p+\nabla\cdot\left\{(\mu+\mu_t)\left(\nabla\vec{u}+(\nabla\vec{u})^T\right)\right\}+\vec{f}\,, \tag{4}$$

where the subscripts l and v denoting the liquid and vapor phases, respectively, and $\dot{m}$ (kg/m^3s) is the phase change rate. In the convention adopted here, the phase change rate $\dot{m}$ is positive for vaporization, and negative for condensation. The derivation of these equations are given in Appendix A and B of [Sato and Niceno, 2013], and will not be reproduced here.

These equations are then discretized using a finite-volume approach. The resulting matrix equations are inverted using the projection method [Chorin, 1968]. Using the color function ϕ to signify the volume fraction of liquid inside any control volume, i.e. a grid cell of the underlying mesh in our case, the average density and viscosity within the volume are respectively defined as follows (i.e. using linear interpolation):

$$\rho=\phi\,\rho_l+(1-\phi)\rho_v \text{ and } \mu=\phi\,\mu_l+(1-\phi)\mu_v. \tag{5}$$

The body-force vector $\vec{f}$ includes both the surface tension and gravity forces. To take into account the effect of buoyancy, the density used for the combined body force $\vec{f}$ is derived as follows:

$$\vec{f}=\vec{f}_{st}+\rho'\vec{g}\,, \tag{6}$$

where $\vec{f}_{st}$ is the surface tension, $\vec{g}$ (m/s^2) the gravitational acceleration vector, and ρ' the average density, which depends on the temperature T, and the respective liquid/vapor content of the cell, as defined by the color function ϕ, as follows:

$$\rho' = \phi\left(\rho_l\big|_{T=T_{sat}} + \left(T - T_{sat}\right)\frac{d\rho_l}{dT}\bigg|_{T=T_{sat}}\right) + \left(1-\phi\right)\left(\rho_v\big|_{T=T_{sat}} + \left(T - T_{sat}\right)\frac{d\rho_v}{dT}\bigg|_{T=T_{sat}}\right), (7)$$

where T_{sat} is the saturation temperature. Note that this is an extension of the familiar Boussinesq approximation to a two-phase flow situation.

Brackbill's Continuum Surface Force (CSF) model [Brackbill *et al.*, 1992] is employed to represent the surface-tension effect. Although the CSF model is widely used for simplicity in modeling, it is known to give rise to unphysical currents in the neighboring fluid; these are called parasitic currents [Jamet *et al.*, 2002]. In order to avoid strong parasitic currents from occurring here, we use the density-scaled form of the model [Brackbill *et al.*, 1992]:

$$\vec{f}_{st} = \sigma\kappa\frac{\nabla\rho}{\left(\rho_l - \rho_v\right)}\frac{\rho}{\left(\rho_l + \rho_v\right)/2}, (8)$$

where σ (*N/m*) is the surface tension coefficient and κ (1/*m*) the curvature, the latter calculated from the local color function distribution in neighboring cells.

A mass-conservative, interface-tracking method based on the color function approach [Nakamura *et al.*, 2001] is employed to delineate the boundaries between the liquid and vapor phases. The transport equation for the color function can be written as:

$$\frac{\partial\phi}{\partial t} + \nabla\cdot\left(\phi\vec{u}\right) = -\frac{1}{\rho_l}\dot{m}, (9)$$

with the rational CIP-CSL2 scheme [Nakamura *et al.*, 2001; Xiao *et al.*, 1996] being adopted for the computation of the advection term. However, in general, other mass-conservative schemes could be used instead. To prevent smearing of the color function, an interface sharpening algorithm [Sato and Niceno, 2012a] is needed. This sharpening process is mandatory, especially for boiling simulations, because the non-divergence-free velocity field (i.e. Eq. (3)) would otherwise smears out the color function. The coupling between the sharpening scheme for the color function used here and the contact angle treatment of the CSF model is described in detail in [Sato and Niceno, 2012b], and will not be repeated here. Briefly, the discretization of the sharpening algorithm is coded in such a way as to ensure that the contact angle treatment is not influenced by the sharpening algorithm, but nonetheless strict mass conservation is maintained.

2.2.   *Energy balance equation*

The thermal energy balance equation is solved under the assumption that the temperature at the liquid-vapor interface is constant, and equal to the ambient saturation temperature, T_{sat}. The governing equation can then be written as follows:

$$C_p\left(\frac{\partial T}{\partial t}+\vec{u}\cdot\nabla T\right)=\nabla\cdot\left(\left(\lambda+\lambda_t\right)\nabla T\right)+Q,\qquad(10)$$

where C_p (J/m^3K) is the specific heat at constant pressure, T (K) is the temperature, λ (W/mK) the thermal conductivity, λ_t (W/mK) the turbulent thermal conductivity, and Q (W/m^3) the volumetric heat source. Using the color function, the specific heat capacity and the thermal conductivity in our model are defined as:

$$C_p=\begin{cases}C_{pl}&\text{for a cell with }\phi\geq0.5\\C_{pv}&\text{for a cell with }\phi<0.5\end{cases}\text{ and }\lambda=\begin{cases}\lambda_l&\text{for a cell with }\phi\geq0.5\\\lambda_v&\text{for a cell with }\phi<0.5\end{cases}.\quad(11)$$

Note that the linear interpolation used for the average cell density, Eq. (5), is not employed for the thermal energy balance equation; this is done in order to capture the jump condition in the material properties. The turbulent thermal conductivity is calculated according to

$$Pr_t=\frac{\mu_t/\rho}{\lambda_t/C_p},\qquad(12)$$

where $Pr_t\left(=0.9\right)$ is the turbulent Prandtl number, assumed to be constant in the present study.

The computational domain consists of both fluid (liquid and vapor) and solid sub-domains, the solid sub-domain being identified using the Immersed Boundary Method (IBM) [Niceno *et al.*, 2013]; conjugate heat transfer between the solid and the fluid is fully taken into account. Because only a flat heat-transfer surface is considered here, it is convenient to position it along a grid line (i.e. a cell face) of the underlying mesh. Of course, use of the IBM approach is then not strictly required in this case, but is retained for the purpose of further generalization of the method.

A special feature of our numerical method for the energy balance equation is the special discretization approach adopted: i.e. usage of an irregular stencil. In order to take into account the temperature of the liquid-vapor interface as T_{sat}, an irregular stencil is used for the discretization, involving the neighboring cells around the interface. We define such cells as the interface cells. With reference to Fig. 2a, the interface cells are identified as follows. First, any cell bisected by the

interface (*i.e.* the surface $\phi = 0.5$) automatically becomes an interface cell. Then the neighboring cells are examined in each co-ordinate direction using the values of the color functions defined at the cell centers. If the quantity $(\phi - 0.5)$ changes sign between the centers, the neighboring cell is also labeled an interface cell. Thus, for the situation illustrated in Fig. 2a, the central cell of the stencil would also be labeled an interface cell. A sample configuration of the interface cells is depicted in Fig. 2b.
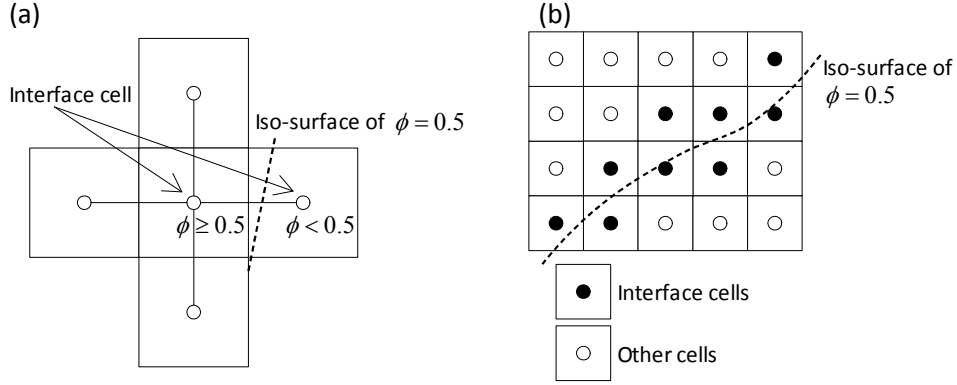
Fig. 2. (a) Definition of the interface cell and (b) sample configuration of the interface cells.

For all non-interface cells, the finite volume method is used. Because the interface is not included in the cells, ordinary discretization schemes can be used: in our case, the second-order-accurate, central-difference scheme is used for the diffusion terms, and the second-order scheme with flux limiter [Roe, 1986] for the advection terms.

For the interface cells, the finite difference method used for the discretization takes into account the saturation temperature at the interface, used as a boundary condition. The scheme works as follows. The advection terms of Eq. (10) are discretized using a first-order upwind algorithm as follows:

$$
\begin{aligned}
\vec{u} \cdot \nabla T &= u\frac{\partial T}{\partial x} + v\frac{\partial T}{\partial y} + w\frac{\partial T}{\partial z} \\
&= \frac{(u+|u|)}{2}\frac{\partial T}{\partial x}\bigg|_{-} + \frac{(u-|u|)}{2}\frac{\partial T}{\partial x}\bigg|_{+} + \frac{(v+|v|)}{2}\frac{\partial T}{\partial y}\bigg|_{-} + \frac{(v-|v|)}{2}\frac{\partial T}{\partial y}\bigg|_{+} \quad (13) \\
&\quad + \frac{(w+|w|)}{2}\frac{\partial T}{\partial z}\bigg|_{-} + \frac{(w-|w|)}{2}\frac{\partial T}{\partial z}\bigg|_{+},
\end{aligned}
$$

where u, v, and w are the velocity component in the x, y and z directions, respectively, $\left.\dfrac{\partial T}{\partial x}\right|_{-}$ and $\left.\dfrac{\partial T}{\partial x}\right|_{+}$ are the temperature gradients on the left ($-$) and right ($+$) sides of the cell center, as explained below. In the staggered arrangement, the velocities are stored at the center of the cell faces, but the velocities at a cell center are used for the discretization; linear interpolation is employed to estimate this velocity. For example, the x-component of the velocity u at the cell center is given as:

$$u_i = \frac{u_{i-1/2} + u_{i+1/2}}{2}, \tag{14}$$

where the subscript i is the cell index in the x direction, and $i \pm 1/2$ is the cell face index as indicated in Fig. 3, which is shown in a one-dimensional representation for the sake of clarity.
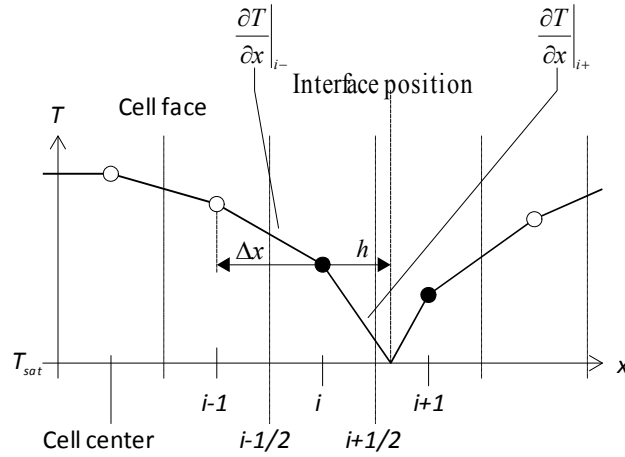

Fig. 3. Discretization of the advection term for the energy balance equation.

The temperature gradients for the interface cell in the x direction are defined as:

$$\left.\frac{\partial T}{\partial x}\right|_{i-} = \begin{cases} \dfrac{T_i - T_{sat}}{h} & \text{if the interface is located between } i\text{-}1 \text{ and } i, \\[2mm] \dfrac{T_i - T_{i-1}}{\Delta x} & \text{otherwise;} \end{cases} \tag{15}$$

9

$$\left.\frac{\partial T}{\partial x}\right|_{i+} = \begin{cases} \dfrac{T_{sat} - T_i}{h} & \text{if the interface is located between } i \text{ and } i+1, \\[2ex] \dfrac{T_{i+1} - T_i}{\Delta x} & \text{otherwise;} \end{cases} \tag{16}$$

where h is the distance between the cell center and the interface position in the x direction, and Δx is the distance between cell centers. $\left.\dfrac{\partial T}{\partial y}\right|_{\pm}$ and $\left.\dfrac{\partial T}{\partial z}\right|_{\pm}$ are calculated in the same manner.

For the discretization of the diffusion term for the interface cell, a second-order-accurate scheme, appropriate to non-uniform grid spacing, is used. For illustration purposes, a sample liquid-vapor interface configuration in two dimensions is shown in Fig. 4. The diffusion term of the cell indexed by (i, j) in Fig. 4a is discretized as:

$$\begin{aligned} \lambda \nabla \cdot \nabla T &= \lambda \left(\left.\frac{\partial^2 T}{\partial x^2}\right|_{i,j} + \left.\frac{\partial^2 T}{\partial y^2}\right|_{i,j} \right) \\[2ex] &= \lambda \left\{ \begin{array}{l} \left(\dfrac{2 T_{i-1,j}}{\Delta x (\Delta x + h_x)} - \dfrac{2 T_{i,j}}{\Delta x h_x} + \dfrac{2 T_{sat}}{h_x (\Delta x + h_x)} \right) \\[2ex] + \left(\dfrac{2 T_{i,j-1}}{\Delta y (\Delta y + h_y)} - \dfrac{2 T_{i,j}}{\Delta y h_y} + \dfrac{2 T_{sat}}{h_y (\Delta y + h_y)} \right) \end{array} \right\}, \end{aligned} \tag{17}$$

where Δx and Δy are the distances between cell centers in the x and y directions, respectively; while h_x and h_y are the distances between cell center and the interface in the x and y directions, respectively. The extension of Eq. (17) to three dimensions is straightforward.
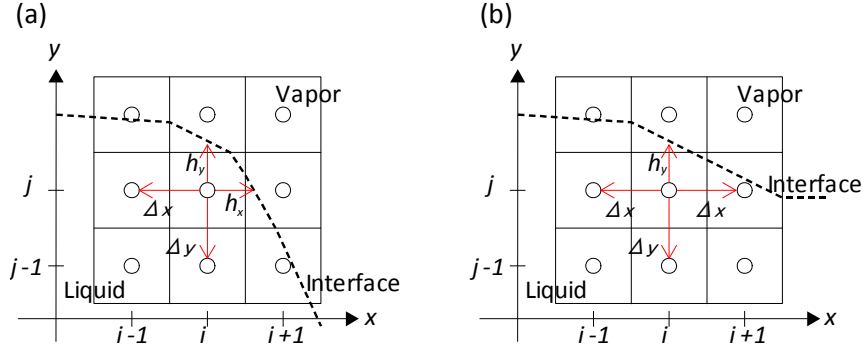
10

Fig. 4. Irregular stencil for diffusion term of energy balance equation and the phase change model.

2.3. *Sharp-interface phase-change model*

The phase-change rate at the liquid-vapor interface is computed directly from the heat fluxes on the two sides, as derived from the separate liquid and vapor phase calculations. The interface is captured using the interface-tracking method (i.e. from the color function distribution), as described earlier. As previously stated, the temperature at the liquid-vapor interface is assumed to be that the saturation temperature at the prevailing pressure, though away from the interface the conditions of superheated liquid and super-cooled vapor are properly taken into account. The phase change rate $\dot{m}_{color}$ at the liquid-vapor interface, as captured by the color function, is modeled as:

$$\dot{m}_{color} = \frac{q_l + q_v}{L} \frac{S_{int}}{V},\tag{18}$$

where q_l and q_v are the heat fluxes (W/m^2) derived from the liquid and the vapor sides of the interface, respectively, L (J/kg) is the latent heat of vaporization, S_{int} (m^2) is the area of the liquid-vapor interface in the computational cell under consideration, and V (m^3) is the cell volume. The heat fluxes to the interface are defined as follows:

$$q_l = \left(\lambda_l + \lambda_t\right)\left(\nabla T_l\right) \cdot \vec{n} \quad \text{and} \quad q_v = -\left(\lambda_v + \lambda_t\right)\left(\nabla T_v\right) \cdot \vec{n},\tag{19}$$

where $\vec{n}$ is the unit normal vector to the interface, pointing from the vapor to the liquid phase. The area S_{int} is calculated by means of the marching cube algorithm [Lorensen and Cline, 1987]. It is to be noted that $\dot{m}_{color}$ is exactly zero for a cell not intersected by the liquid-vapor interface. More details of the phase-change model are given in Ref. [Sato and Niceno, 2013].

11

2.4. *Nucleation-site model*

Here, only *heterogeneous nucleation* [Carey, 2007], i.e. nucleation at the interface between the liquid phase and solid phase, is taken into account. An additional model would be needed to simulate *homogeneous nucleation* [Carey, 2007], in which bubble nucleation takes place completely within the superheated liquid; this type of nucleation process is not considered here.

The modeling for a *single* nucleation site had been proposed earlier by the authors [Sato and Niceno, 2015], in this work, the location of the nucleation site was prescribed *a priori* on the heat-transfer surface, together with a nucleation activation temperature T_{act}. When the temperature at the nucleation site reached this temperature, a small vapor bubble (seed bubble) was placed at the site. The seed bubble was assumed to be initially hemi-spherical in shape, the radius being typically one cell width of the underlying grid. This means that the model is dependent on the discretization (grid spacing) adopted, and a grid refinement study was then required to evaluate the influence of this assumption on the model predictions.

The *single* nucleation site model has since been extended to encompass a *multiple* nucleation site model [Sato and Niceno, 2017]. In this model, each nucleation site has its ID number, and the location and the activation temperature T_{act} are prescribed *a priori* for each nucleation site. When the wall temperature at the nucleation site reaches T_{act}, a small vapor bubble (seed bubble) is placed at the site. This procedure is identical to the single nucleation site model. The key points in the multiple nucleation site model are how to define the location and the activation temperature.

Each location of the nucleation site is selected using a non-biased random number generator, in order to distribute the nucleation sites on the heat-transfer surface without examining the micro-scale imperfections of the surface. The *linear congruential random number generator* [Press *et al.*, 1988] is employed for this purpose, for convenience, since it is already implemented into the C/C++ programming languages as default; our code is written in C++.

The nucleation activation temperature T_{act} is obtained from the available experimental data for the nucleation site density as a function of the wall temperature, an example being illustrated in Fig. 5. In this Figure, the vertical axis is the number of nucleation sites, which is the product of the nucleation site density (m^{-2}) and the area of the heat-transfer surface (m^2) in the computational domain. The temperature $T_{act, \#1}$ is read off from the trendline, at which the value on the vertical axis is 1; i.e. $T_{act, \#1}$ is defined as the activation temperature of the nucleation site of ID = #1. This process continues with $T_{act, \#2}$, and proceeds until

the activation temperature reaches T_{max}, which is chosen to be higher than the expected wall temperature computed in the simulation.
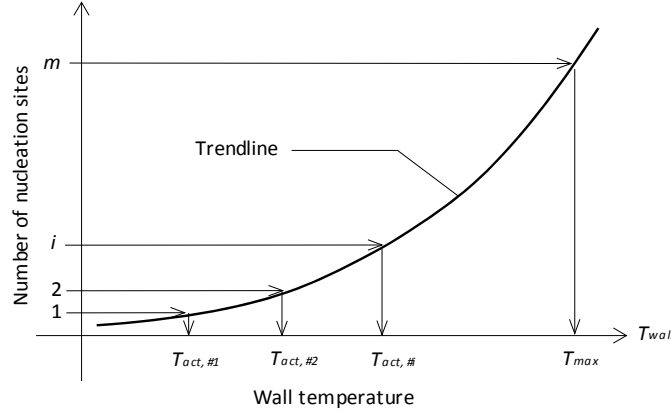

Fig. 5. The number of nucleation sites as a function of wall temperature T_{wall}.

An example of a set of nucleation sites generated using the above-mentioned procedure will be shown in Sec. 3.3. It is to be recalled that these nucleation sites are identified in a pre-process-manner (i.e. before the CFD simulation begins), and the locations and associated activation temperatures thus determined do not subsequently change during the simulation.

In the case when one needs to simulate nucleate boiling without recourse to the relevant experimental data, a correlation for the nucleation site density, for example that of Kocamustafaogullari [1983] or Hibiki and Ishii [2003], based on surface condition of heat-transfer surface, can be used instead.

2.5. *Micro-layer model*

The depletable micro-layer model, including the wall-adhesion model developed earlier by the authors [Sato and Niceno, 2015], is reported here. The model is a necessary addition to the cell-wise CFD simulation required to resolve the phase-change phenomena taking place in the thin liquid film (micro-layer) beneath each growing bubble. If one were to incorporate the physics of the micro-layer directly into the CFD simulation, the disparity in cell size would render the calculation unfeasible. Hence, a micro-layer model of some description is necessary.

In the context of the depletable micro-layer model, the micro-layer thickness δ (m) is treated as a variable stored at the center of *wall-adjacent cells* (i.e. the fluid cells next to the wall). The temperature at the liquid-vapor interface above the micro-layer is assumed to be constant, and equal to the saturation

temperature, T_{act}, at the ambient pressure. Also, we assume that the liquid in the micro-layer is stagnant (i.e. it can be vaporized at its upper surface, but the motion of the liquid beneath this may be regarded as unimportant to the physics of the vaporization process). Based on these assumptions, the heat flux through the micro-layer, q_{ml} (W/m^2), may be expressed simply as:

$$q_{ml} = \lambda_l \left(\frac{T_w - T_{sat}}{\delta} \right), \tag{20}$$

where λ_l (W/Km) is the thermal conductivity of the liquid (water), and T_w (K) is the local wall-surface temperature. The interfacial phase-change rate of the micro-layer, $\dot{M}_{ml}$ ($kg/m^2 s$), can be written as:

$$\dot{M}_{ml} = \frac{q_{ml}}{L} . \tag{21}$$

The Navier-Stokes solver requires an estimate of the phase-change rate per unit volume, $\dot{m}_{ml}$ ($kg/m^3 s$), defined as:

$$\dot{m}_{ml} = \dot{M}_{ml} \frac{S_v}{V} , \tag{22}$$

where S_v (m^2) is the vapor area on the heat-transfer surface in the corresponding computational cell. The phase change rate calculated from the micro-layer model, $\dot{m}_{ml}$, is then added to that arising from the liquid-vapor interface indicated by the color function, $\dot{m}_{color}$, which is captured on the scale of the CFD mesh, to produce the total mass transfer rate as follows:

$$\dot{m} = \dot{m}_{color} + \dot{m}_{ml} . \tag{23}$$

The summation expressed in Eq. (23) is computed for each computational cell.

The thickness of the micro-layer decreases as a result of vaporization, and the rate of decrease can be described in the direction normal to the heat-transfer surface as:

$$\frac{d\delta}{dt} = -\frac{1}{\rho_l} \dot{M}_{ml} . \tag{24}$$

In order to incorporate this feature into the current algorithm, an Euler explicit method is employed for the time discretization of Eq. (24) as follows:

$$\frac{\delta^{n+1} - \delta^n}{\Delta t} = -\frac{1}{\rho_l} \dot{M}_{ml}^n , \tag{25}$$

where the superscript n denotes the current time step, $n+1$ the advanced time step, and Δt (s) the time increment.

14

With this modeling strategy, numerical difficulties could occur in the case of too large a phase-change rate, occasioned by a vanishingly small value of the denominator in Eq. (20). In order to avoid this singularity in the solution procedure, we introduce the concept of a *minimum micro-layer thickness*: δ_{min}. When the solution of Eq. (25), or for the micro-layer thickness at the advanced time, δ^{n+1}, falls below δ_{min}, it is fixed at δ_{min}, and no further vaporization is deemed to occur in that cell. The definition of δ_{min} is equivalent to the assumption of the *adsorbed film thickness* in the physical description of the layers, as described in Ref. [Wayner Jr, 1982]. In the present work, δ_{min} is set to a very small value, $\delta_{min} = 1.0 \times 10^{-9}$ m, and is subsequently used for all the simulations presented in this chapter. Note that δ_{min} is set for computational convenience only, and is small enough not to have an influence on the computed bubble growth rate, since 1.0×10^{-9} m is smaller than the size of a water molecule.

In the micro-layer model developed earlier by the authors [Sato and Niceno, 2015], the initial micro-layer thickness δ_0 was defined as:

$$\delta_0 = C_{slope} r_L , \qquad (26)$$

where C_{slope} is constant, obtained either from measurement or via numerical experiments, and r_L (m) is the horizontal distance from the nucleation site to the cell center of the wall-adjacent cell containing the triple line; see Fig. 6.
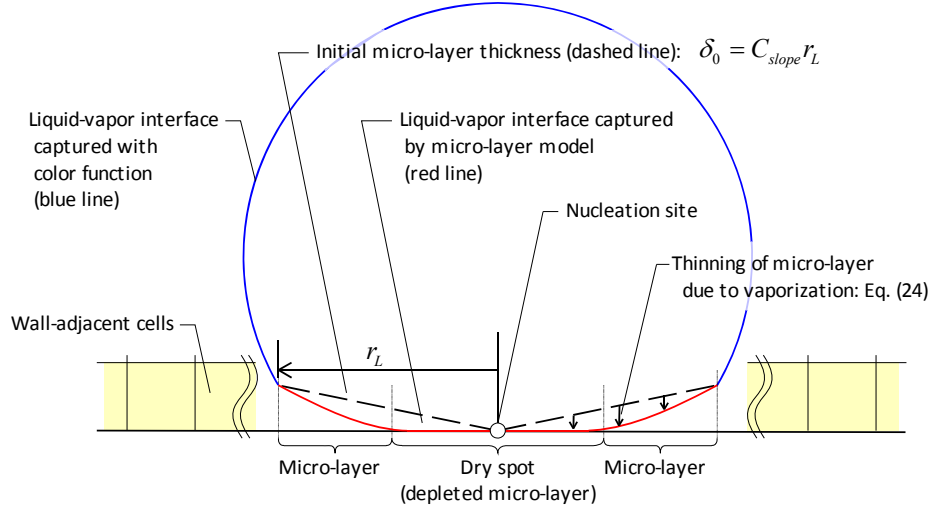

Fig. 6. The distance r_L from the nucleation site to the wall-adjacent cell containing the triple line.

The linear modeling assumption in Eq. (26) is based on the observations of Utaka *et al.* [2013]. Thus, for example, $C_{slope} = 4.46 \times 10^{-3}$ for water, and

$C_{slope} = 1.02 \times 10^{-2}$ for ethanol, in each case describing boiling from a heated quartz glass surface at atmospheric pressure. Further, C_{slope} appears to be almost independent of the applied heat flux [Utaka *et al.*, 2013]. In our model, we consider that C_{slope} depends on the material and surface-roughness properties of the heat-transfer surface, as well as on the ambient pressure. Thus, when we simulate nucleate boiling with an unknown combination of working fluid, material properties, surface-roughness and pressure, we first perform a parameter study to determine C_{slope} in such a way that the bubble growth rate agrees with the corresponding measurement. The procedure for water at atmospheric pressure would be then as follows:

Step 1. Carry out a first simulation with $C_{slope} = 4.46 \times 10^{-3}$, the observed value [Utaka *et al.*, 2013].

Step 2. Compare the computed bubble growth rate between simulation and experiment. If the two are in good agreement, an appropriate C_{slope} is assumed to have been obtained. Otherwise, go to Step 3.

Step 3. Use a modified estimate of C_{slope} and repeat the simulation. According to our experiences, a smaller value of C_{slope} results in faster bubble growth, and vice versa. This enables the modification to be made in the right direction. Then return to Step 2 and test for agreement.

To find an appropriate C_{slope} more systematically, one could use an optimization algorithm, such as one based on the Newton-Raphson method, and this option will be explored in future, to accelerate the convergence process.

Regarding the wall-adhesion force, the model used here is based on the CSF model of Brackbill *et al.* [1992], and the specific details applied to the micro-layer model are described in [Sato and Niceno, 2015]. Briefly, referring to Fig. 7, the curvature κ around the outer extremity of the micro-layer in the physical situation, as shown in Fig. 7 (left), is approximated by setting $\theta_{eq} = 0$ in the CSF model, as shown in Fig. 7(right), and the surface tension force calculated from the resulting curvature is applied to the apparent contact line.
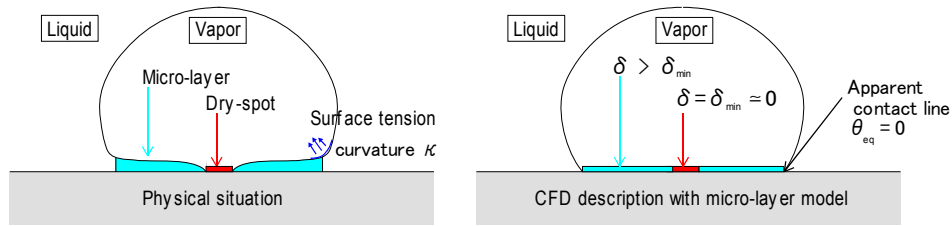

Fig. 7. Wall-adhesion force acting on the apparent contact line based on the CSF model.

It should be emphasized that the value of C_{slope} is the only empirical parameter in our model, which is thus much more straightforward than for other existing micro-region models [Stephan and Busse, 1992; Lay and Dhir, 1995] in which several unknown parameters – such as the dispersion constant, the adsorbed film thickness, the gradient of the micro-layer film thickness at the extremities of the micro-region – all need to be assigned appropriate values.

The status of a particular nucleation site (i.e. activated or non-activated) is set as follows: a nucleation site is activated (i.e. a seed bubble is planted) if the temperature at the site exceeds the value T_{act}, and the site is situated in the liquid phase of the fluid domain. Once the site is activated, the seed bubble is planted and starts growing. The activated nucleation site is deactivated when the site is again situated in the liquid phase (i.e. the bubble detaches). This site is reactivated again if T_w exceeds the T_{act} appropriate to this site. Consequently, a stream of bubbles can issue from the same site, and this is true for all such nucleation sites on the heat transfer surfae.

2.6. *The complete solution algorithm*

With each of the component parts in the model, as described above, in place, we can now outline the complete solution procedure.

Step 1. Generate the nucleation sites (Sec. 2.4) and set initial conditions;

Step 2. Start the time loop;

Step 3. Calculate the total mass transfer rate $\dot{m}$ via Eq. (23);

Step 4. Calculate the body force $\vec{f}$ from Eq. (6);

Step 5. Update the local velocities and pressure using the projection method using Eq. (1) and Eq. (4);

Step 6. Update the color function ϕ from Eq. (9);

Step 7. Create a primordial seed bubble at each newly activated nucleation site according to the prescription given in Sec. 2.4;

Step 8. Update the temperature field T using Eq. (10);

Step 9. Advance to the next time step, loop back to Step 3, and continue till the end of simulation.

The time increment Δt, which is limited both by the CFL condition given in Eq. (4.84) of Anderson [1995], and by the stability condition for the surface tension treatment through Eq. (61) in [Brackbill *et al.*, 1992], is defined as follows:

$$\Delta t = \min\left(C_{CFL} \frac{\Delta x}{|\vec{u}|_{max}}, C_{st} \left(\frac{\rho_v \Delta x^3}{2\pi\sigma} \right)^{\frac{1}{2}} \right),\qquad(27)$$

where C_{CFL} and C_{st} are dimensionless constants representing respective safety factors for the two explicit formulations. The first term represents the limitation imposed by the CFL condition, and $C_{CFL} = 0.25$ is adopted for all the computations reported here. The second term represents the limitation due to the surface tension modeling. In the original CSF model [Brackbill *et al.*, 1992], this term is given as $\left(\frac{\bar{\rho}\Delta x^3}{2\pi\sigma} \right)^{\frac{1}{2}}$, in which $\bar{\rho} = (\rho_l + \rho_v)/2$. However, according to our experience, numerical instabilities ensue when this definition is applied. Thus, we use ρ_v instead of $\bar{\rho}$ in Eq. (27). Since $\rho_v \ll \bar{\rho}$, this represents a severe limitation on the maximum time increment, but simultaneously effectively resolves the numerical instability issue. However, the resulting limitation on Δt imposes unaffordable restrictions on our available computer resources. Since the time increment limitation of $\left(\frac{\bar{\rho}\Delta x^3}{2\pi\sigma} \right)^{\frac{1}{2}}$ results directly from the explicit treatment of the surface tension force in Eq. (4) [Brackbill *et al.*, 1992; Rudman, 1998; Hysing, 2006; Herrmann, 2008; Galusinski and Vigneaux, 2008; Raessi *et al.*, 2009; Liovic *et al.*, 2010], a semi-implicit [Hysing, 2006; Raessi *et al.*, 2009] or implicit [Denner and van Wachem, 2015] treatment could mitigate the restrictive time-step constraint. However, the implementation of such models is a subject for future research. Thus, from a purely pragmatic perspective, we circumvent the problem by increasing the Δt defined in Eq. (27) by applying a multiplication factor $C_{st} = 10$; no numerical instability problems have been encountered, as so this factor was applied for all the subsequent computations.

2.7. *Assumptions*

The assumptions used in the numerical method are summarized here, for clarity. First, we assume that the working fluid is incompressible. Second, the temperature at the liquid-vapor interface remains constant, and equal to the saturation temperature at the prevailing pressure. As a result, the coefficient of surface tension between liquid and vapor is constant at a value determined again by the saturation temperature, and the Marangoni effect may be neglected. Also, radiation heat-transfer is not taken into account, which may limit the accuracy of the computation in the film-boiling regime, especially for the high wall-temperature case.

18

In the nucleation site model, we assume that each nucleation site has a specific nucleation activation temperature T_{act}. When the wall temperature of the nucleation site reaches its activation temperature, a hemispherical vapor seed bubble is artificially placed at that location.

In the micro-layer model, the slope of the initial micro-layer thickness, C_{slope}, is assumed to be independent of the heat flux, but dependent on the material of the heat transfer surface and the prevailing pressure.

3. Simulations

One verification test case, and two validation cases are presented here. The verification case is a three-dimensional simulation of a growing vapor bubble in a superheated liquid, the computed results being compared against an analytical solution. The first validation case refers to nucleate pool boiling from a single nucleation site. The temperature distribution on the heat-transfer surface is compared between that measured in experiment and that calculated in the simulation; the measured and calculated bubble growth rates are also compared. The second validation case is derived from a series of pool boiling tests involving multiple nucleation sites under different applied heat-fluxes. The applied heat flux ranges from 50 to 1500 kW/m^2, covering the boiling regimes of the nucleate boiling, Departure from Nucleate Boiling (DNB) and the film boiling.

3.1. *Verification of phase-change model*

The phase-change model has been verified for one-dimensional, phase-change problems, and a one-dimensional spherically symmetric problem of a growing vapor bubble in a superheated liquid under zero gravity [Sato and Niceno, 2013], through simulated using a 3D Cartesian grid. Here we present the spherically symmetric case. A spherical vapor bubble is initially at saturation temperature T_{sat}, and located in a superheated liquid of temperature $T_\infty > T_{sat}$. The bubble grows as a consequence of the heat flux from the liquid phase to the vapor bubble surface. This growing bubble problem was solved analytically by Scriven [1959], and has since been used as a verification test for phase-change CFD codes by Son [2001], Kunkelmann and Stephan [2009], Akhtar and Kleis [2011] and Tanguy *et al.* [2014]. The analytical solution is based on the assumption of laminar flow.

The working fluids are water and steam at a system pressure of 101.3 kPa. The liquid superheat, $\Delta T_\infty = T_\infty - T_{sat}$, is set at 1.25, 2.5 or 5.0 K. The initial bubble diameter is set at 50 μm, and the simulations were continued until the

bubble radius reaches 100 μm. Cubic cells of 1.95, 0.98 and 1.95 μm are used for the computation of ΔT_∞ = 1.25, 2.5 and 5.0 K, respectively.

Three-dimensional views of the bubble shape for the case $\Delta T = 5.0\,K$ at initiation, and at $t = 0.066\,ms$, are shown in Fig. 8. It can be noticed that the vapor bubble grows, but keeps spherical shape. The radius of the growing bubble is compared with the analytical solution of Scriven [1959] in Fig. 9. The results computed using the phase-change model show good agreement with the analytical solutions.
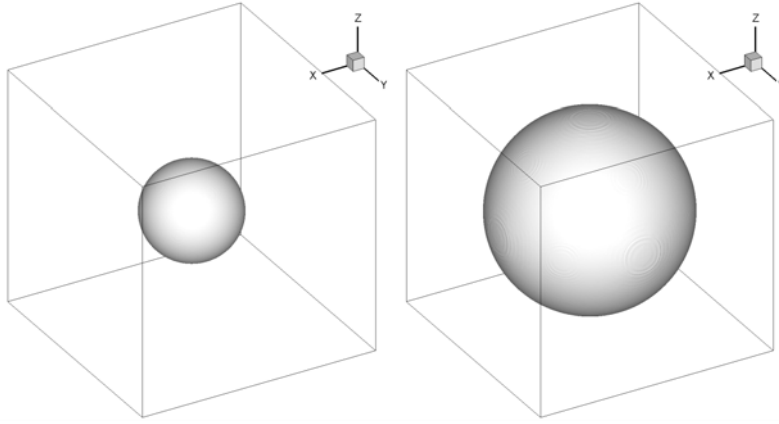
Fig. 8. Initial spherical bubble shape (left), and bubble shape at $t = 0.066\,ms$ (right).
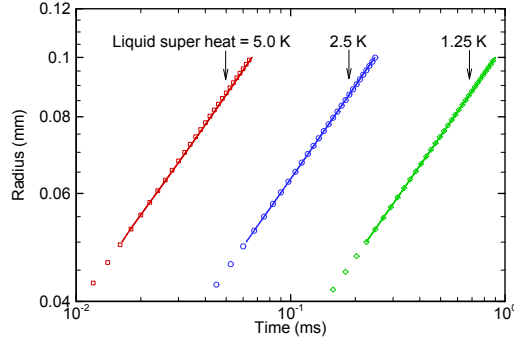
Fig. 9. Comparison of the growing-bubble radius between computations (lines) and analytical solutions (symbols) for different degrees of superheat.

3.2. *Pool boiling from a single-nucleation site*

The first validation test case is the simulation of the experiment carried out by Yabuki and Nakabeppu [2014]. Isolated bubbles, created under saturated,

nucleate-pool-boiling conditions, were measured at atmospheric pressure. The working fluid was water at atmospheric pressure. A Micro-Electro-Mechanical System (MEMS) sensor was used for the temperature measurement, together with an High Speed Video (HSV) camera. The experimental set-up is shown in Fig. 10 (top). A glass cell of inner dimension $10\ mm \times 10\ mm$ was positioned over the MEMS sensor. A thin film heater was attached to the bottom of the sensor. The heat flux produced by the heater ranged from 30 to $39\ kW/m^2$. A tiny hydrogen bubble was generated (using electrolysis of the water) to act as a bubble nucleus, and the temperature was subsequently measured at several locations away from the nucleation site; see Fig. 10 (bottom). The MEMS sensor cannot measure the absolute value of the temperature, except at a few isolated points. Hence, the "relative temperature" was only reported in [Yabuki and Nakabeppu, 2014]. The equilibrium contact angle was also measured, and was judged to be between $10°$ and $15°$.
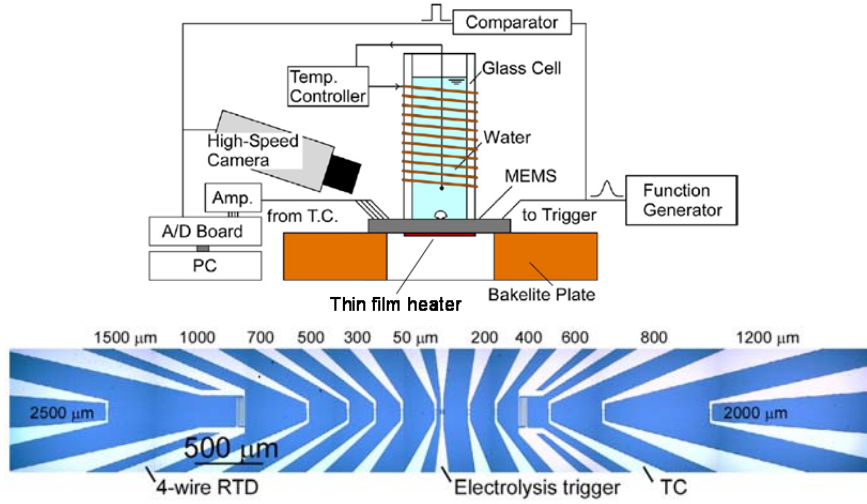

Fig. 10. Schematic of the set-up of the Yabuki and Nakabeppu's experiment (top), and an image of the MEMS sensor for the temperature measurement and electrolysis trigger (bottom) [Yabuki and Nakabeppu, 2014].

The conditions of simulation were set in the same way as in the experiment: the nucleation activation temperature $T_{act} = 115.3\ °C$, the applied heat flux $q'' = 39\ kW/m^2$. A silicon substrate thickness of $0.18\ mm$ was included in the computational domain as a solid, and the constant heat flux was applied to the bottom surface of the substrate. The computational fluid domain size is $5\ mm$ in both lateral directions, and $20\ mm$ in the vertical direction. Assuming symmetry, one fourth of the bubble is computed. The total number of computational cells is

9 million (144 × 144 × 448), cubic cells of 31 μm being used for the fluid domain. The parameter for the initial thickness of the micro-layer C_{slope} is set to 4.46×10^{-3}, which is identical to the value measured by Utaka *et al.* [2013]. No turbulence model was included in this test case, since the cell size is small enough for Direct Numerical Simulation (DNS) to be employed. Full details of the simulation is reported by Sato and Niceno [2015], together with a case with a different applied heat flux.

The computed bubble shape is compared visually against photographic data taken during the experiment in Fig. 11. Good optical agreement is observed for the entire duration of the test, from initial bubble growth to its departure from the solid surface. To examine the bubble growth rate in more quantitative terms, the time history of the bubble principal dimensions are compared against measured values in Fig. 12. The base diameter is the diameter of the bubble on the heat-transfer surface, and the lateral diameter is the maximum bubble dimension in the lateral direction. As can be seen, there is very good agreement between calculation and experiment, and consistent with the photographic and numerically generated images displayed in Fig. 11.
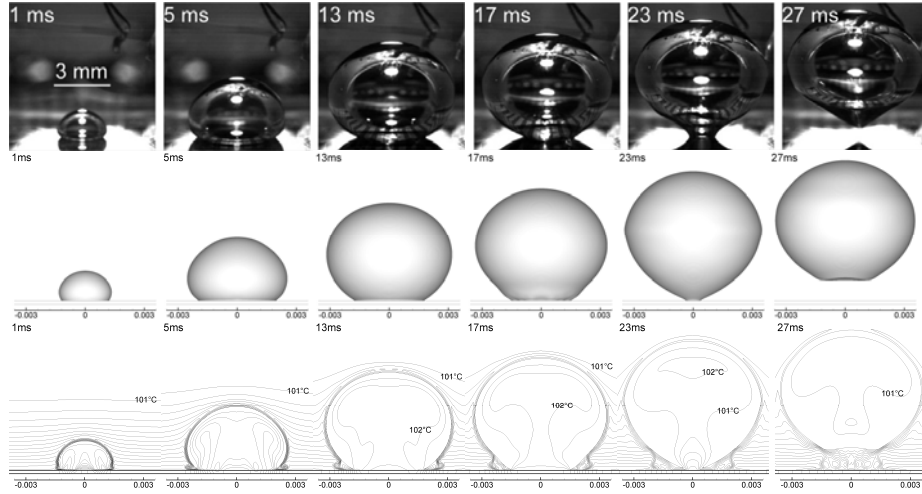

Fig. 11. Comparison of the evolution of the bubble shape between experiment [Yabuki and Nakabeppu, 2014] (top) and simulation (middle), and the computed isotherms with an interval of 1 *K* (bottom).
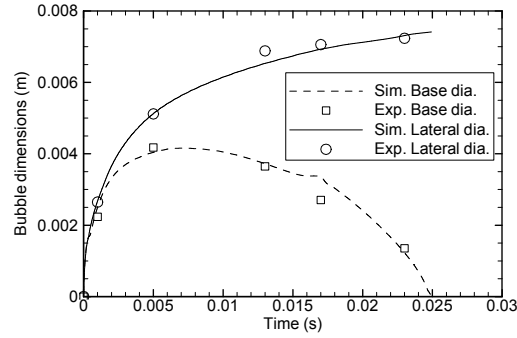
Fig. 12. Comparison of bubble principal dimensions between experiment [Yabuki and Nakabeppu, 2014] and simulation.

The computed temperature field is compared with measurement in Fig. 13. In general, computed results follow similar trends to those observed in the test. In the computation, several spikes are observed, which derive from the very thin micro-layer just before its depletion: i.e. the singularity caused by the small value of δ in Eq. (20). The computed temperature at 1500 μm from the nucleation site is obviously lower than the measurement for the entire duration of the bubble cycle. This particular measurement point may not have been covered by the micro-layer in the experiment (though this cannot be confirmed from the reported data), although it was covered according to the simulation.
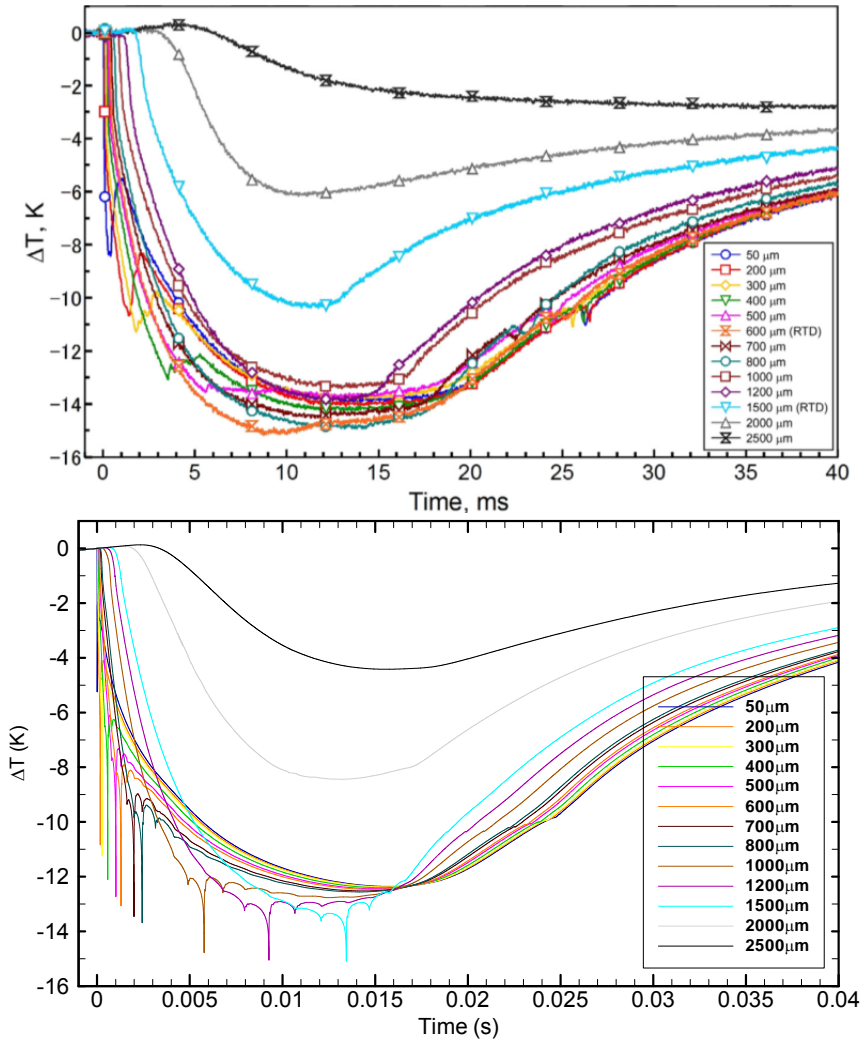
Fig. 13. Comparison of relative temperature over the heat-transfer surface between measurement [Yabuki and Nakabeppu, 2014] (top) and simulation (bottom).

Other validation test cases for the nucleate pool boiling from a single nucleation site are given in Ref. [Sato and Niceno, 2015], in which the evolution of bubble dimensions and temperature field over the heat-transfer surface are compared with measurements. In general, good agreement was obtained between the simulations and the experiments, indicating the applicability of the micro-layer model to nucleate pool boiling simulations.

3.3.   *Pool boiling from multiple nucleation sites*

The second validation case is simulation of the experiment of Gaertner [1965]. The experiment relates to saturated pool boiling of water from a heated horizontal plate at atmospheric pressure. Two types of solid surface material were employed over a base copper block: platinum and copper. The range of heat fluxes was from $q'' = 16\ kW/m^2$ to $1600\ kW/m^2$, which covers the nucleate boiling regime, Departure from Nucleate Boiling (DNB), and the film boiling regime. The heat fluxes and temperatures within the copper block were measured, and the number of active nucleation sites was also counted; results are presented in Fig. 14. Here, the wall superheat ΔT is defined as $T_w - T_{sat}$, where T_w is the temperature at the heat transfer surface and T_{sat} is the saturation temperature at the ambient (atmospheric) pressure. In Gaertner's experiment, the nucleation site density was measured up to a wall temperature of $T_w = 115.2\ ˚C$. In addition to the plots presented in Fig. 14, several photos of the boiling water were taken via a side window in the tank. In the numerical study, the experiment utilizing the copper surface is employed as the validation case, since the measurement database is then more comprehensive.
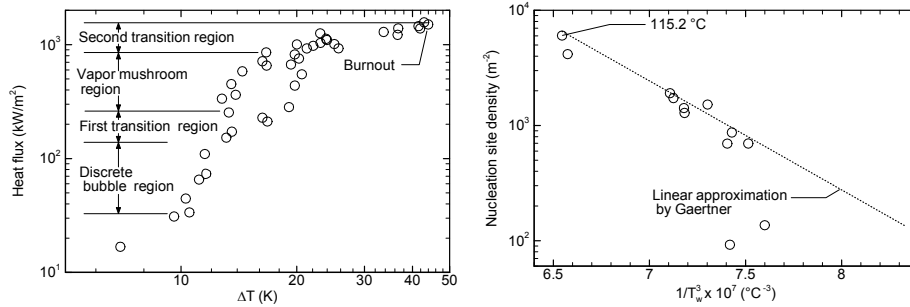

Fig. 14. Experimental results of Gaertner [1965]: heat flux as a function of wall superheat (left), and nucleation site density as a function of the inverse of the cube of the wall temperature (right).

3.3.1.   *Conditions for the simulation*

The conditions for the CFD simulation are set appropriately to mirror the parameters set in Gaertner's experiments. The physical properties of water, steam and copper used in the simulations are listed in Table 1. The system pressure is set at atmospheric ($1.013 \times 10^5\ Pa$). The computational domain consists of both fluid and solid regions, as illustrated in Fig. 15. Small and large computational domains have been prepared, as shown in the Figure. For the small domain,

periodic boundary conditions are applied to the side boundaries, this in order to keep the computational domain smaller and thereby to save on the number of cells. The small domain is considered to be applicable to the pool boiling simulations in which convection from outside of the heater region to the inside has small influence on the heat transfer, i.e. for the low applied heat-flux case. The large computational domain mirrors the actual experimental set-up, in which a cylindrical heater is installed at the center of the tank, though is at a reduced scale. The small computational domain is 20 *mm* × 20 *mm* × 16 *mm* in length, width and height, respectively, the upper 10 *mm* representing the fluid domain, and the lower 6 *mm* the copper block. The large computational domain is 40 *mm* × 40 *mm* × 38 *mm*, the upper 32 *mm* representing the fluid domain, and the lower 6 *mm* the solid domain. In the solid domain, a cylindrical-shaped copper block of diameter 20 *mm* locates at the center, and the surrounding solid material is the thermal insulation, for which the thermal conductivity is defined to be zero. The diameter of the copper block used in the experiment was 50.8 *mm*, however we cannot compute this dimension because of computational power limitations.

The feasibility of the reduction of the heater diameter from 50.8 *mm* to 20.0 *mm* is considered here, especially from the viewpoint of instability of the vapor phase on the heat-transfer surface, the so-called Rayleigh-Taylor instability. If the length of the liquid-vapor interface is smaller than the critical wave length λ_c, the interface is stable, resulting in stable film boiling [Ishii and Hibiki, 2011]. Otherwise, the interface is unstable. The critical wave length λ_c is defined as:

$$\lambda_c = 2\pi \sqrt{\frac{\sigma}{(\rho_l - \rho_v)g}} \ . \qquad (28)$$

In the case of water at saturation under atmospheric pressure, $\lambda_c = 15.8$ *mm*. This indicates that vapor over a heat-transfer surface of diameter either 20.0 *mm* or 50.8 *mm* would be unstable. Thus the modeling of the heater diameter as 20.0 *mm* is considered to be feasible in the present context.

The potential nucleation sites, chosen according to the pre-processing algorithm described in Sec. 2.4, are distributed over the heat-transfer surface, as depicted in Fig. 15, and are signified by the small, colored spherical dots. It will be recalled that the locations of the nucleation sites are chosen using a random number generator, and are therefore not uniformly distributed over the surface. The nucleation activation temperature for each site is defined in such a way that the nucleation site density matches that measured in the experiment. For this purpose, a trendline derived from the linear inverse cube line drawn in Fig. 14 (right) is utilized.

Table 1. Physical properties of water at atmospheric pressure (101.3 kPa), and those of the copper block beneath.

	Density	Viscosity	Heat capacity	Thermal conductivity	Latent heat	Surface tension
	(kg/m^3)	(Pa s)	(J/kgK)	(W/mK)	(J/kg)	(N/m)
vapor	0.597	1.26×10^{-5}	2030	0.025	2.26×10^6	5.90×10^{-2}
liquid	958.4	2.80×10^{-4}	4216	0.679		
copper	8960	–	385	401	–	–
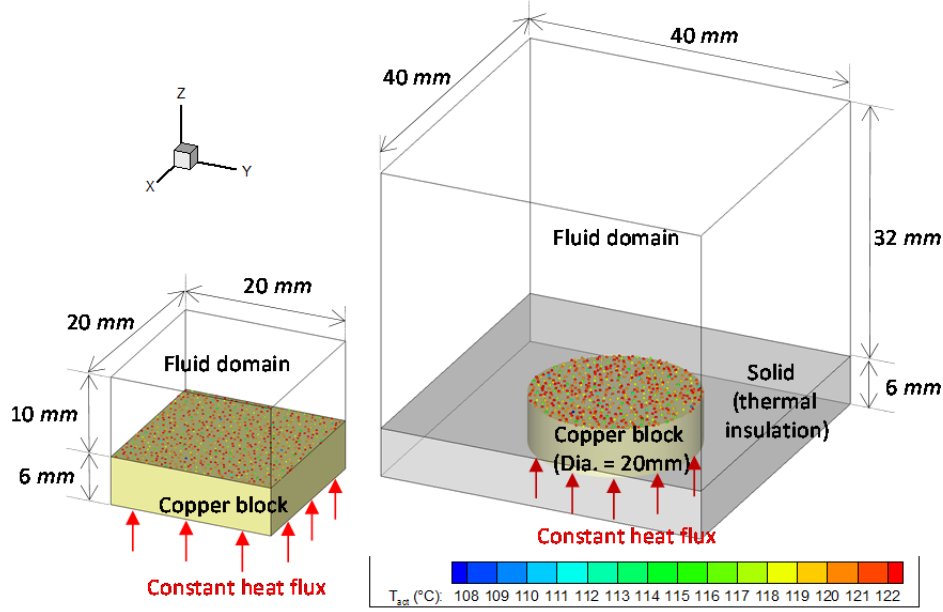
Fig. 15. Computational domain for the simulation of Gaertner's pool-boiling experiments [Gaertner, 1965]. Left figure is the small computational domain for low applied heat flux in which a periodic boundary condition is applied to the side boundaries. Right figure is the large domain for the higher heat flux case, which mirrors the experimental set-up.

The computational grid for the small domain consists of $160 \times 160 \times 128$ (= 3'276'800) cells, in length, width and height, respectively. The number of grids for the large domain is $224 \times 224 \times 320$ (= 16'056'320) cells. In both cases, cubic cells of dimensions 125 μm are used for the fluid domain. High-aspect-ratio cells are used in the solid domain, with the minimum cell height for the solid

27

cells adjacent to the fluid domain set at 30 μm in order to accurately capture the local temperature gradient, and thereby the surface heat flux.

For the calculation, the copper block is assumed to be uniformly heated over its bottom surface, with a constant normal heat flux prescribed as a boundary condition. Eight simulation cases, with different heat fluxes, have been considered using the small computational domain: i.e. $q'' = 50$, 100, 150, 200, 300, 400, 500 and 600 kW/m^2. The large computational domain is used for the simulations of $q'' = 600$, 800, 1000, 1200 and 1500 kW/m^2. A non-slip boundary condition is imposed at the fluid-solid interface, whether this be liquid/solid or vapor/solid in origin. The top plane of the fluid domain is the outlet boundary for the velocity field, and a Dirichlet boundary condition is adopted for the temperature field at this plane: $T = T_{sat}$. The boundary condition at the sides of the computational domain is periodic for the small domain, and adiabatic, no-slip walls for the large domain.

The entire fluid domain is initially filled with liquid, with the flow velocity set to zero everywhere. In prescribing the initial temperature field, one could assume $T = T_{sat}$ throughout both the fluid and solid domains, and then apply the heat flux at time $t = 0$, mimicking the carefully prescribed conditions at initiation in Gartner's experiments. However, to accelerate the progress to steady-state, and purely for reasons of computational convenience, the following prescription is employed instead. The temperature is set to T_{sat} everywhere in the liquid except for a layer of thickness 0.5 mm above the heated surface: here, it is assumed there is a linear transition to an initial estimate of the averaged wall temperature – a value in this case taken directly from experimental measurement. A linear temperature variation is again assumed for the solid domain, derived from conditions necessary to sustain the constant applied heat flux q''. Since the simulation will be continued until pseudo-steady-state conditions have been attained, the ultimate influence of the initial conditions on the final simulation results is considered to be minor.

3.3.2. *Results of the simulations*

Parameter studies for C_{slope} were first undertaken to obtain the most appropriate value, then, the boiling simulations from multiple nucleation sites were subsequently carried out.

Parameter studies for C_{slope}

In the depletable micro-layer model employed here [Sato and Niceno, 2015], the most appropriate value for C_{slope} should be adopted for the subsequent computer simulations, as already explained in Sec. 2.5. According to the measurements of

Utaka *et al*. [2013], a value of $C_{slope} = 4.46 \times 10^{-3}$ is appropriate for water boiling from a heated quartz glass surface at atmospheric pressure. In contrast, platinum and copper surfaces were featured in Gaertner's experiments [Gaertner, 1965]. Since C_{slope} is considered here to be dependent on the material properties of the heat-transfer surface, a parametric study of the effects of varying the assumed value of C_{slope} appears to be unavoidable in a systematic study of the issue. Consequently, four simulation cases with different values of C_{slope} have been carried out to assess the effect: $C_{slope} = 1.11 \times 10^{-2}$, 1.56×10^{-2}, 2.01×10^{-2} and 2.45×10^{-2}. The heat flux given at the base of the solid domain in each case was fixed at $q'' = 100\ kW/m^2$. The small computational domain is used for this study. The simulations were then continued until a cut-off time of $t = 0.12\ s$, the time at which two or three bubble cycles from each nucleation site had taken place.

In the experiment of Gaertner [1965], the bubble diameter at departure was measured photographically for each applied heat flux, as indicated in Fig. 16a. On average, all the measured bubble diameters at departure were similar (3 *mm*), and this was in good agreement with the correlation of Fritz [1935], though the error bars on the experimental data are admittedly rather large. The bubble diameters at departure computed using the simulation model reported here for different assumed values of C_{slope} are compared with experimental measurement in Fig. 16b. Here, the applied heat flux in the experiment was measured at $107\ kW/m^2$, and though not identical to that used in the simulation ($100\ kW/m^2$), comparisons of results are considered feasible, since the influence of the actual magnitude of the heat flux on the bubble departure diameter is small, as can be observed in Fig. 16a, notwithstanding the error bars on the measurements, of course. In Fig. 16b, the displayed error bars of the simulation results are the standard deviations of the bubble departure diameters computed from more than 14 bubbles. As can be seen, the average bubble diameter changes from 4 *mm* to 3 *mm* for the range of $C_{slope} = 1.11 \times 10^{-2}$ to $C_{slope} = 2.54 \times 10^{-2}$, but all predictions are well within the uncertainties in the experimental data. Due to this fact, it is not straightforward to define the most appropriate value of C_{slope}. However, we have selected $C_{slope} = 2.54 \times 10^{-2}$ from the viewpoint of absolute agreement with the average value from Fig. 16b. Hereafter, $C_{slope} = 2.54 \times 10^{-2}$ has been adopted for all the simulations reported here.
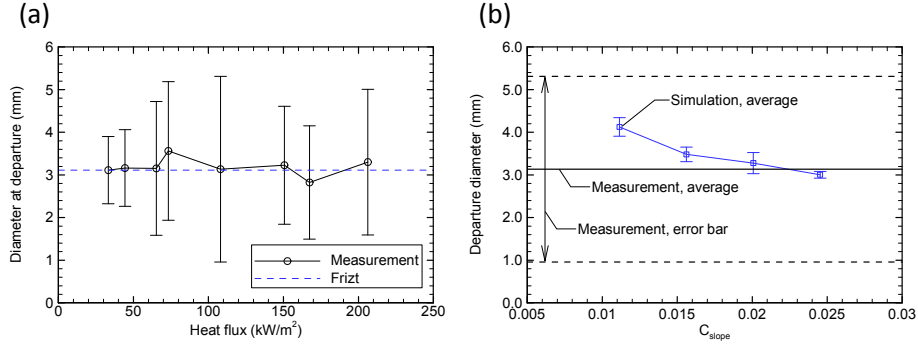
Fig. 16. (a) Bubble departure diameters measured by Gaertner [1965], and (b) comparison of departure diameters according to measured data for different assumed values of C_{slope}.

Wall temperature and heat flux

As a consequence of the above parameter studies, our simulations of nucleate pool boiling were subsequently carried out using the value $C_{slope} = 2.54 \times 10^{-2}$. The simulations were continued until a pseudo-steady-state or saturation had been established, and an asymptotic temperature within the copper block had been attained. The average time increment Δt are 3.3 μs for $q'' = 50$ kW/m^2, 1.0 μs for $q'' = 400$ kW/m^2, and 0.5 μs for $q'' = 1200$ and 1500 kW/m^2. Time histories of the wall temperature T_w for the different applied heat fluxes are displayed in Fig. 17. The simulation cases using the small computational domain are shown on the left, and on the right those obtained using the large computational domain.

The average wall temperature approaches an asymptotic value in all cases, except for $q'' = 1500$ kW/m^2. The computation for $q'' = 1500$ kW/m^2 was interrupted when the wall temperature reached 145 °C, the temperature at which the heater burned out in the experiment.

The simulation case for $q'' = 600$ kW/m^2 is computed using both the small and large domains: the average temperatures were 116.5 °C and 116.8 °C, respectively. The very small differences between these two simulations authenticates the use of the small domain for this flow situation.
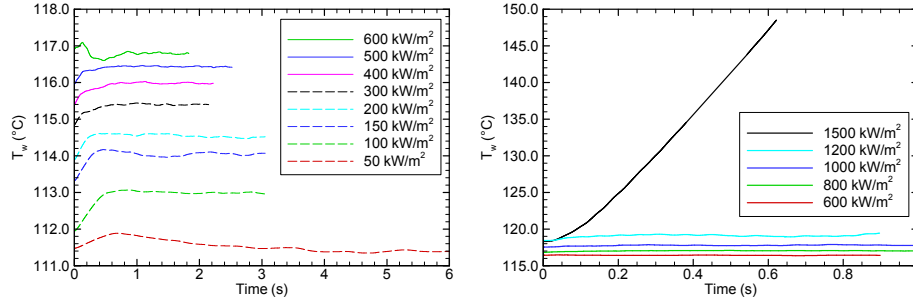
30

Fig. 17. Time histories of the calculated wall temperature T_w based on the small computational domain (left) and the large domain (right).

Heat transfer coefficient

Comparisons of the overall heat transfer coefficient measured in the experiment [Gaertner, 1965] and that calculated are shown in Fig. 18. The wall superheat is defined as $T_w - T_{sat}$. The computed results using the small and large domains are depicted separately in this figure. The applied heat fluxes for the small computations are $q'' = 50, 100, 200, 300, 400, 500$ and $600 \, kW/m^2$, while those for the large domain are $q'' = 600, 800, 1000, 1200$ and $1500 \, kW/m^2$. The case $q'' = 600 \, kW/m^2$ is computed for both domains. As can be seen, the difference between them is very small. The measured data is scattered; the reason for this remains unclear. In general, the simulation results agree well with measurement, and lie within the scattering of the measurement data.
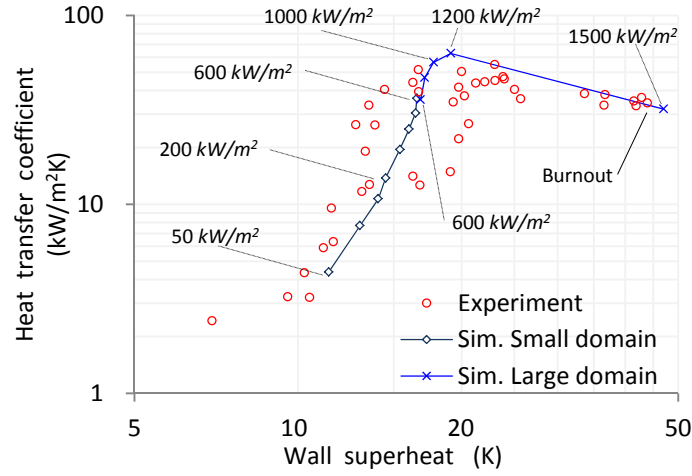
31

Fig. 18. Comparison of overall heat transfer coefficient between the experiment [Gaertner, 1965] and simulation.

In the present simulations, a database trendline of the nucleation site density as a function of the wall temperature is necessary in prescribing the nucleation-site activation temperatures. The trendline measured by Gaertner [1965] is available up to $T_w = 115.2\,°C$ for nucleate boiling at atmospheric pressure (Fig. 14 (right)). The highest value of T_w computed in the simulations undertaken here was $145\,°C$, this for $q'' = 1500\,kW/m^2$. As a consequence, extrapolation of the measured tabled results was used in the simulation.

Sources of mass transfer: superheated liquid and micro-layer

The time-averaged ratios of the two mass transfer rates arising from the *super-heated liquid* and the *micro-layer* are displayed in Fig. 19(a) as functions of the applied heat flux. As illustrated schematically in Fig. 19(b), the *super-heated liquid* contribution derives principally from the vaporization process driven by the superheated liquid surrounding the bubble, as well as from the *micro-layer* vaporization occurring beneath the bubble. Time-averaging had been taken over the period at which pseudo-steady-state conditions have been established. Since the pseudo-steady-state condition cannot be achieved for $q'' = 1500\,kW/m^2$, the result for this case is not included in this figure. As can be seen, the *micro-layer* contribution increases with increasing applied heat flux, and reaches 90% of the total mass transfer rate for $q'' = 1200\,kW/m^2$.
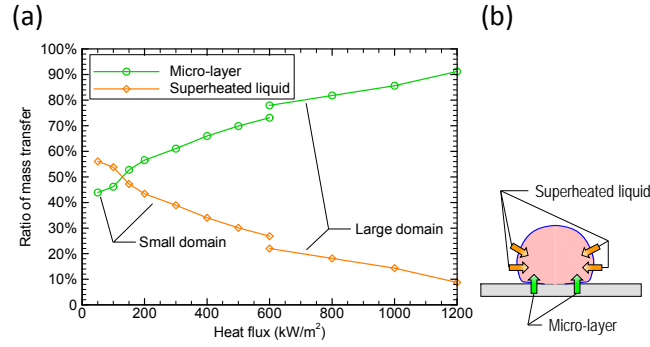
Fig. 19. (a) Relative partitioning of the two contributions to the total mass transfer rate as functions of the applied heat flux, and (b) a schematic of where the different mass transfer mechanisms originate.

Bubble shape and temperature distribution

The bubble shapes and the temperature distributions at pseudo-steady-state are presented in Fig. 20 for the cases $q'' = 50$, 100 and 400 kW/m^2. For clarity, the temperature distributions are based on two different color contour maps: one for the solid and the other for the fluid. In the cases $q'' = 50$ and 100 kW/m^2, isolated bubbles are generated, and superheated liquid can be observed. For the case $q'' = 400 \, kW/m^2$, larger numbers of nucleation sites are activated as a consequence of the higher wall temperatures, and the bubbles ultimately merge through overcrowding. Large vapor bubbles immerge of sizes in excess of 10 mm above the primordial bubbles growing on the wall surface at the nucleation sites.
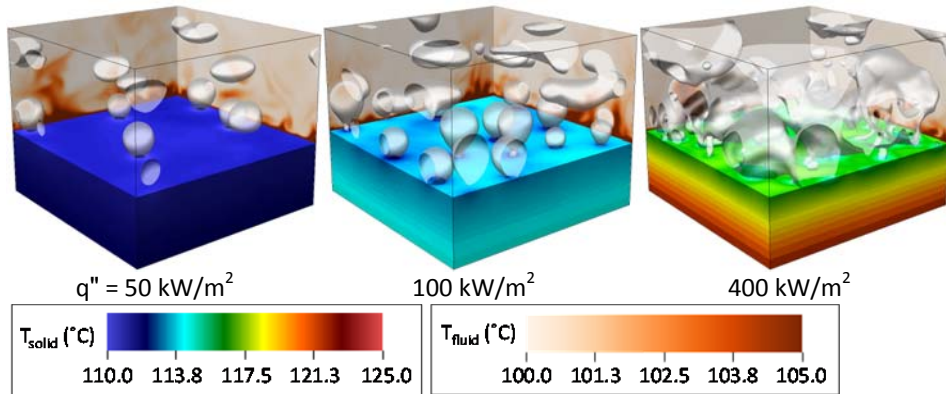

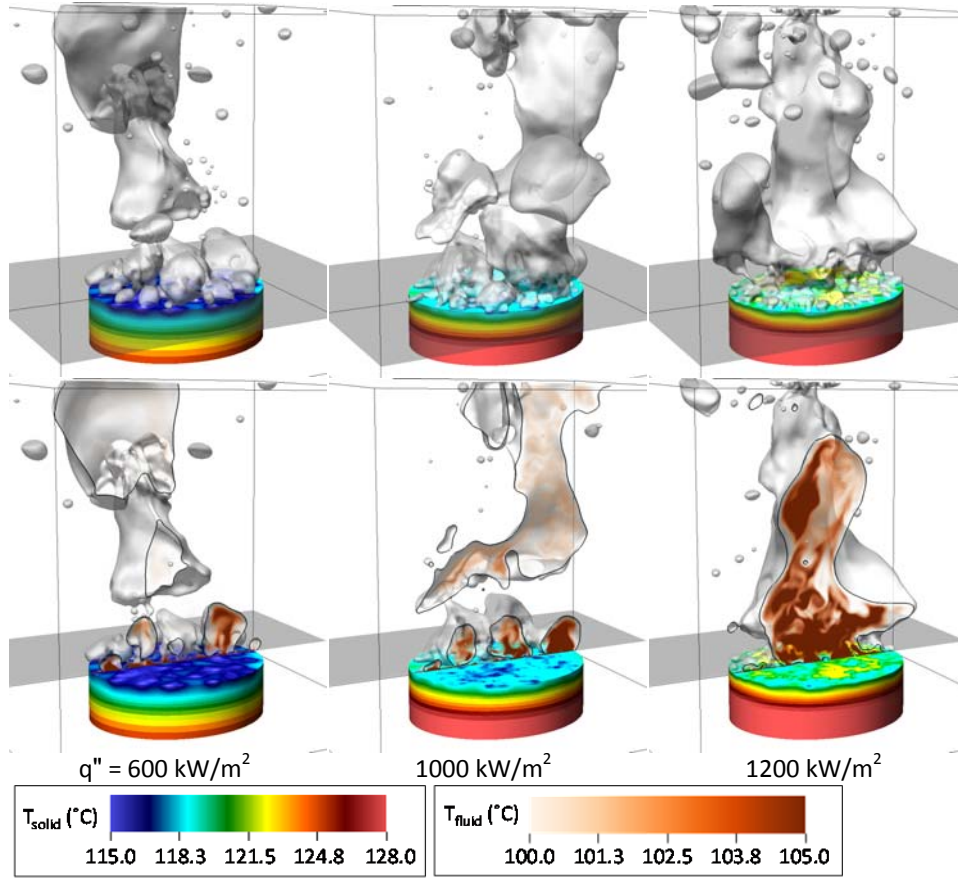Fig. 20. Schematics showing the bubble shape and temperature distributions throughout the fluid/solid domains.

33

Fig. 21. Computed bubble shape and temperature distributions for the case $q'' = 600$ kW/m^2 (left column), 1000 kW/m^2 (middle column), and 1200 kW/m^2 (right column). Figures in each column are snapshots at a same instant.

Figure 21 shows the computed flow field for the higher applied heat flux cases: $q'' = 600$ kW/m^2 (left column), 1000 kW/m^2 (middle column), and 1200 kW/m^2 (right column). Figures in each column are snapshots at a same instant. Bubbles in the entire domain are shown in the top row, while bubbles only in a half domain are depicted in the bottom row to visualize the temperature distribution on the heat-transfer surface and in the fluid domain T_{fluid}. T_{solid} in this figure is the temperature of the surface of the cylindrical copper block. With increase of the applied heat-flux, a larger area of heat transfer surface is covered with the vapor phase. The temperature distribution over the heat-transfer surface is not homogeneous, even though the copper block has a high thermal conductivity, and a thickness of 6 mm.

34

Comparing T_{fluid} in Fig. 20 and Fig. 21, the superheated liquid cannot be clearly seen in Fig. 21, even though the temperature at the heat-transfer surface is higher than that in Fig. 20. The reason for this is considered to be due to convective flow around the heat-transfer surface, which prevents the growth of the thick thermal boundary layer in the liquid phase. The temperature field in the vapor phase for $q'' = 1200 \, kW/m^2$ (Fig. 21(bottom-right)) shows evidence of turbulent flow conditions.

The flow field for $q'' = 1500 \, kW/m^2$ at $t = 0.5 \, s$ is shown in Fig. 22. The heat-transfer surface is already fully covered by the vapor phase. The temperature over the heat-transfer surface is more than $140\,^{\circ}C,$ that in the peripheral region being slightly lower than elsewhere. The liquid superheat cannot be seen in the bulk, since the heat-transfer surface is mostly covered by vapor, and liquid does not make contact with the wall for which the temperature is higher than T_{sat}. Figure 22c shows the distribution of the micro-layer thickness, for which the dry parts of the surface are colored white. Clearly, most of the heat-transfer surface is in a dry condition, and the small area where micro-layer exists is at a lower temperature than that observed in Fig. 22b.
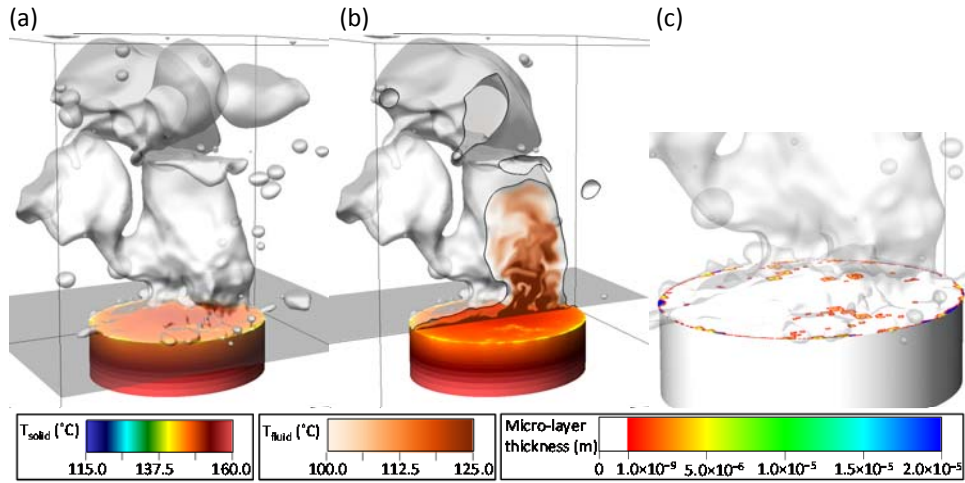

Fig. 22. Computed flow field for the case $q'' = 1500 \, kW/m^2$ at $t = 0.5$ s: (a) bubble shape in the entire domain and the T_{solid} distribution; (b) those in the half domain, together with the temperature distribution in fluid T_{fluid} on the center plane (middle); and (c) the distribution of the micro-layer thickness over the heat-transfer surface.

Evolution of the flow and temperature fields around DNB for $q'' = 1200 \, kW/m^2$ are displayed in Fig. 23. The images in the top two rows depict the changing bubble shape and the evolving distribution of temperature in the

solid T_{solid}, over a period from $t = 694\ ms$ to $754\ ms$, at intervals of $12\ ms$. The two middle rows show the evolution of the micro-layer thickness during the same period. The time history of the heat flux is shown in Fig. 23 (bottom-left). The *total* heat flux is partitioned into three component contributions: that arising from (i) vaporization of the micro-layer, (ii) single-phase liquid heat transfer, and (iii) single-phase vapor heat transfer, respectively. The origins of these different mechanisms are illustrated in schematic form in Fig. 23 (bottom-right).

Returning to the top two rows in Fig. 23, a large bubble is seen to detach from the heat-transfer surface at the time signified by image (a), and subsequently new large bubble is generated during the time-sequence (b)-(e), which ultimately detaches as seen in image (f). The result of these processes on the micro-layer thickness indicates that the area of the dry-patch (colored white) expands slightly during the sequence (b) to (d), at which time the heat-transfer surface is covered by the large vapor bubble.

Referring now to the evolution of the heat flux during this period Fig. 23 (bottom-left), the contribution to the heat flux from the *micro-layer*, and from *single-phase liquid* heat transfer, are at similar levels of around $600\ kW/m^2$, while the *single-phase vapor* heat flux is insignificant. These combine to result in a *total* heat flux that oscillates in time, and the peaks appear around the time-sequences represented in the images labeled (a) and (f). Note that the oscillation of the *total* heat flux is synchronized with that of the *single-phase liquid* heat flux.

From these results, one can conclude that the oscillation in the *total* heat flux is largely influenced by the *single-phase vapor* heat transfer, and the peak of the *total* and *single-phase vapor* heat fluxes appears when the large bubble, which covers the entire heat-transfer surface, detaches from it.
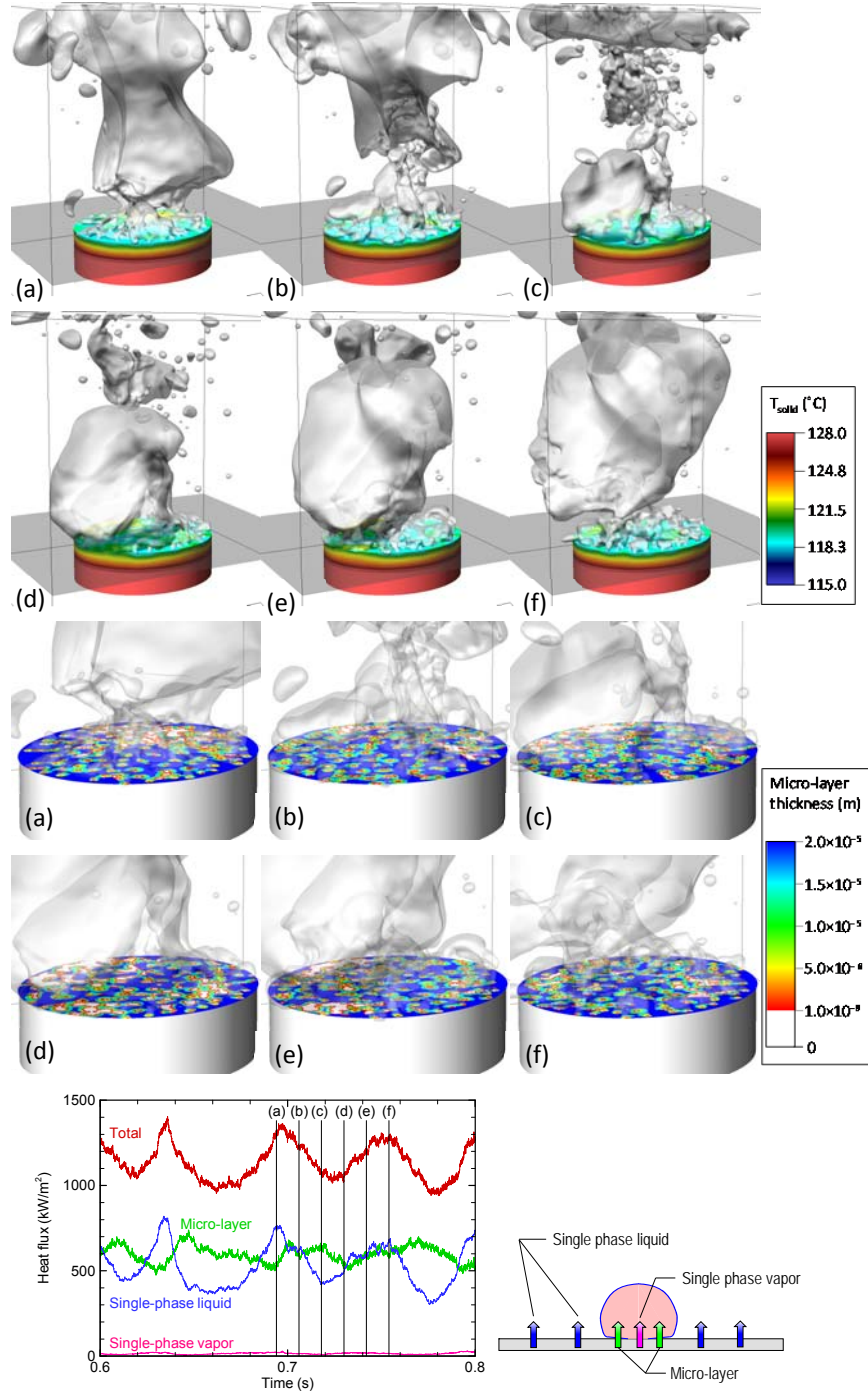
36

Fig. 23: Evolution of vapor bubbles and temperature distribution on the copper block (top), distribution of micro-layer thickness (middle) and heat flux partitioning between the various components (bottom), for the case $q'' = 1200 \ kW/m^2$.

Photographic study comparisons

The computed bubble shape for $q'' = 100$, 600, 1000 and 1200 kW/m^2 are compared with the photos taken during the respective experiments [Gaertner, 1965] in Fig. 24. It is not straightforward to compare the snapshots quantitatively, since the depth of the field of view in the photos is not known, and the diameter of heat-transfer surface is different in the experiment than in the simulation. However, qualitatively at least, the computed bubble shapes and those observed do display a measure of similarity.
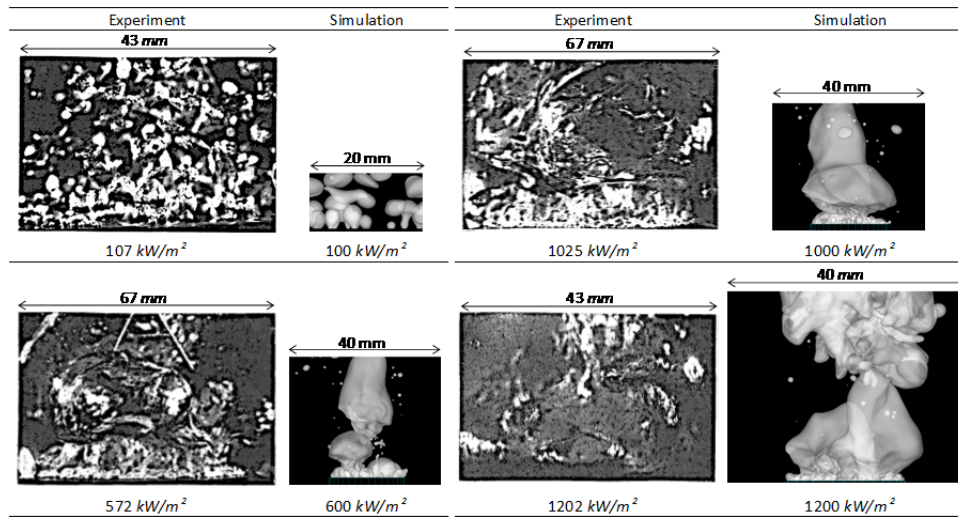

Fig. 24. Comparison of bubble shape between experiment and simulation. Note that the diameter of heat-transfer surface is 50.8 *mm* for the experiment and 20 *mm* for the simulation.

4.   Closure

In this Chapter, we have presented a series of CFD simulations for pool boiling as an example of two-phase heat-transfer. These simulations are computed using the numerical methods developed by the authors. If one needs to overview the CFD simulation for boiling flow, such review articles can be found in the Encyclopedia of Two-Phase Heat Transfer and Flow II Volume 4. Our numerical method is based on an interface-tracking method, and modeling of the micro-layer beneath the growing bubble and identification of typical nucleation sites are built in. Our *depletable micro-layer model* can treat the vaporization process occurring within the micro-layer. Nucleate boiling is initiated from a number of specified nucleation sites, the locations of which are prescribed initially, assuming homogeneity of the heat transfer surface, the specific site locations

being defined using an unbiased random-number generator. Each potential nucleation site is activated or not in the subsequent CFD simulation according to its prescribed activation temperature, data for which are derived from experiment. Conjugate heat transfer between solid and fluid domains is fully taken into account, and the interface tracking model is incorporated to follow the subsequent bubble development and ultimate detachment from the heated surface.

A series of pool boiling simulations was carried out with different applied heat fluxes from 50 to 1500 kW/m^2 for which measurement data are available for comparison. All the simulation cases, except that for 1500 kW/m^2, were continued until pseudo-steady-state conditions had been attained, in order to accurately extract the time-averaged data. Since the time increment employed in the simulations is of the order of microseconds, millions of time steps are needed to reach these conditions. However, having undertaken this process, and averaging the numerical data predictions, the computed temperatures at the heat-transfer surface are seen to agree well with those measured in the experiments, meaning that the overall heat transfer coefficient had been accurately predicted by the CFD simulations without the use of multiple empirical correlations. The simulation case with 1500 kW/m^2 was interrupted when the wall temperature reached 145 $°C$, the temperature at which the heater burned out in the experiment.

Although the numerical method can predict the heat transfer coefficient accurately, and reproduce the bubble shapes, there still remains an issue related to the micro-layer. The parameter value C_{slope} is obtained through comparison with experiments, and it is not calculated from a governing equation based on physics. With the present effort being the complete understanding of the micro-layer formation process, we consider it is necessary to utilize Direct Numerical Simulation (DNS) throughout. Only then will all the governing equations be derived from physics. A further step would be the development of a similar numerical method applicable to convective boiling conditions.

Acknowledgments

References

Akhtar, M.W., Kleis, S.J. (2011). A volume of fluid phase change model on adaptive octree grids, *J. ASTM Int.*, **8**.
Anderson, J. (1995). *Computational fluid dynamics*. (McGraw-Hill Education).

Brackbill, J.U., Kothe, D.B., Zemach, C. (1992). A continuum method for modeling surface tension, *J. Comput. Phys.*, **100**, pp. 335-354.

Carey, V.P. (2007). *Liquid-vapor phase-change phenomena*, Second Ed. (Taylor & Francis).

Chorin, A.J. (1968). Numerical solution of the Navier-Stokes equations, *Math. Comp.*, **22**, pp. 745-762.

Denner, F., van Wachem, B.G.M. (2015). Numerical time-step restrictions as a result of capillary waves, *J. Comput. Phys.*, **285**, pp. 24-40.

Fritz, W. (1935). Berechnung des Maximalvolume von Dampfblasen, *Phys. Z.*, **36**, pp. 379-388.

Gaertner, R.F. (1965). Photographic study of nucleate pool boiling on a horizontal surface, *J. Heat Trans.*, **87**, pp. 17-27.

Galusinski, C., Vigneaux, P. (2008). On stability condition for bifluid flows with surface tension: Application to microfluidics, *J. Comput. Phys.*, **227**, pp. 6140-6164.

Harlow, F.H., Welch, J.E. (1965). Numerical calculation of time-dependent viscous incompressible flow of fluid with free surface, *Phys. Fluids*, **8**, pp. 2182-2189.

Herrmann, M. (2008). A balanced force refined level set grid method for two-phase flows on unstructured flow solver grids, *J. Comput. Phys.*, **227**, pp. 2674-2706.

Hibiki, T., Ishii, M. (2003). Active nucleation site density in boiling systems, *Int. J. Heat and Mass Trans.*, **46**, pp. 2587-2601.

Hirt, C.W., Nichols, B.D. (1981). Volume of fluid (VOF) method for the dynamics of free boundaries, *J. Comput. Phys.*, **39**, pp. 201-225.

Hysing, S. (2006). A new implicit surface tension implementation for interfacial flows, *Int. J. Numer. Meth. Fluids*, **51**, pp. 659-672.

Ishii, M., Hibiki, T. (2011). *Thermo-Fluid Dynamics of Two-Phase Flow*. (Springer New York).

Jamet, D., Torres, D., Brackbill, J.U. (2002). On the theory and computation of surface tension: The elimination of parasitic currents through energy conservation in the second-gradient method, *J. Comput. Phys.*, **182**, pp. 262-276.

Jawurek, H.H. (1969). Simultaneous determination of microlayer geometry and bubble growth in nucleate boiling, *Int. J. Heat and Mass Trans.*, **12**, pp. 843-848.

Kocamustafaogullari, G. (1983). Pressure dependence of bubble departure diameter for water, *International Communications in Heat and Mass Transfer*, **10**, pp. 501-509.

Koffman, L.D., Plesset, M.S. (1983). Experimental observations of the microlayer in vapor bubble growth on a heated solid, *J. Heat Trans.*, **105**, pp. 625-632.

Kunkelmann, C., Stephan, P. (2009). CFD simulation of boiling flows using the volume-of-fluid method within OpenFOAM, *Numer. Heat Trans., Part A*, **56**, pp. 631 - 646.

Lal, S., Sato, Y., Niceno, B. (2015). Direct numerical simulation of bubble dynamics in subcooled and near-saturated convective nucleate boiling, *Int. J. Heat and Fluid Flow*, **51**, pp. 16-28.

Lay, J.H., Dhir, V.K. (1995). Shape of a vapor stem during nucleate boiling of saturated liquids, *J. Heat Trans.*, **117**, pp. 394-401.

Liovic, P., Francois, M., Rudman, M., Manasseh, R. (2010). Efficient simulation of surface tension-dominated flows through enhanced interface geometry interrogation, *J. Comput. Phys.*, **229**, pp. 7520-7544.

Lorensen, W., Cline, H. (1987). Marching cubes: A high resolution 3D surface construction algorithm, *SIGGRAPH '87: Proceedings of the 14th Annual Conference on Computer Graphics and Interactive Techniques*, **21**, pp. 163-169.

Mukherjee, A., Dhir, V.K. (2015) *Encyclopedia of Two-Phase Heat Transfer and Flow II*, Numerical Modeling of Vapor Bubbles During Nucleate Boiling and Slug Flow, (World Scientific Publishing), pp. 111-139.

Murallidharan, J., Giustini, G., Sato, Y., Ničeno, B., Badalassi, V., Walker, S.P. (2016). Computational fluid dynamic simulation of single bubble growth under high-pressure pool boiling conditions, *Nuclear Engineering and Technology*, **48**, pp. 859-869.

Nakamura, T., Tanaka, R., Yabe, T., Takizawa, K. (2001). Exactly conservative semi-Lagrangian scheme for multi-dimensional hyperbolic equations with directional splitting technique, *J. Comput. Phys.*, **174**, pp. 171-207.

Niceno, B., Reiterer, F., Ylönen, A., Prasser, H.M. (2013). Simulation of single-phase mixing in fuel rod bundles, using an immersed boundary method, *Phys. Scripta*, **88**.

Press, W.H., Flannery, B.P., Teukolsky, S.A., Vetterling, W.T. (1988). *Numerical recipes in C: the art of scientific computing*. (Cambridge University Press).

Raessi, M., Bussmann, M., Mostaghimi, J. (2009). A semi-implicit finite volume implementation of the CSF method for treating surface tension in interfacial flows, *Int. J. Numer. Meth. Fluids*, **59**, pp. 1093-1110.

Roe, P.L. (1986). Characteristic-based schemes for the Euler equations, *Annu. Rev. Fluid Mech.*, **18**, pp. 337-365.

Rudman, M. (1998). A volume-tracking method for incompressible multifluid flows with large density variations, *Int. J. Numer. Meth. Fluids*, **28**, pp. 357-378.

Sato, Y., Niceno, B. (2012a). A conservative local interface sharpening scheme for the constrained interpolation profile method, *Int. J. Numer. Meth. Fluids*, **70**, pp. 441-467.

Sato, Y., Niceno, B. (2012b). A new contact line treatment for a conservative level set method, *J. Comput. Phys.*, **231**, pp. 3887-3895.

Sato, Y., Lal, S., Niceno, B. (2013). Computational fluid dynamics simulation of single bubble dynamics in convective boiling flows, *Multiphase Sci. Tech.*, **25**, pp. 287-309.

Sato, Y., Niceno, B. (2013). A sharp-interface phase change model for a mass-conservative interface tracking method, *J. Comput. Phys.*, **249**, pp. 127-161.

Sato, Y., Niceno, B. (2015). A depletable micro-layer model for nucleate pool boiling, *J. Comput. Phys.*, **300**, pp. 20-52.

Sato, Y., Niceno, B. (2017). Nucleate pool boiling simulations using the interface tracking method: Boiling regime from discrete bubble to vapor mushroom region, *International Journal of Heat and Mass Transfer*, **105**, pp. 505-524.

Scriven, L.E. (1959). On the dynamics of phase growth, *Chem. Eng. Sci.*, **10**, pp. 1-13.

Sharp, R. (1964). The nature of liquid film evaporation during nucleate boiling. Lewis Research Center, Ohio, USA.

Smagorinsky, J. (1963). General circulation experiments with the primitive equations, *Mon. Weather Rev.*, **91**, pp. 99-164.

Son, G. (2001). A numerical method for bubble motion with phase change, *Numer. Heat Trans., Part B*, **39**, pp. 509-523.

Stephan, P.C., Busse, C.A. (1992). Analysis of the heat transfer coefficient of grooved heat pipe evaporator walls, *Int. J. Heat and Mass Trans.*, **35**, pp. 383-391.

Tanguy, S., Sagan, M., Lalanne, B., Couderc, F., Colin, C. (2014). Benchmarks and numerical methods for the simulation of boiling flows, *J. Comput. Phys.*, **264**, pp. 1-22.

Utaka, Y., Kashiwabara, Y., Ozaki, M. (2013). Microlayer structure in nucleate boiling of water and ethanol at atmospheric pressure, *Int. J. Heat and Mass Trans.*, **57**, pp. 222-230.

Voutsinos, C.M., Judd, R.L. (1975). Laser interferometric investigation of the microlayer evaporation phenomenon, *J. Heat Trans.*, **97**, pp. 88-92.

Wayner Jr, P.C. (1982). Adsorption and capillary condensation at the contact line in change of phase heat transfer, *Int. J. Heat and Mass Trans.*, **25**, pp. 707-713.

Xiao, F., Yabe, T., Ito, T. (1996). Constructing oscillation preventing scheme for advection equation by rational function, *Computer Physics Communications*, **93**, pp. 1-12.

Yabuki, T., Nakabeppu, O. (2014). Heat transfer mechanisms in isolated bubble boiling of water observed with MEMS sensor, *Int. J. Heat and Mass Trans.*, **76**, pp. 286-297.

Youngs, D.L. (1982) *Numerical methods for fluid dynamics*, ed. J.Baines, K.W.M.a.M. (Ed.), Time-dependent multi-material flow with large fluid distortion, (Academic Press, New York), pp. 273-285.

41